UCRL-16089

University of California

Ernest O. Lawrence Radiation Laboratory

A MEASUREMENT OF THE POLARIZATION
OF SIGMA-ZERO HYPERONS PRODUCED BY PI-MINUS MESONS
ON HYDROGEN NEAR 1.3 BeV/c

TWO-WEEK LOAN COPY

This is a Library Circulating Copy which may be borrowed for two weeks. For a personal retention copy, call Tech. Info. Division, Ext. 5545

Berkeley, California

DISCLAIMER

This document was prepared as an account of work sponsored by the United States Government. While this document is believed to contain correct information, neither the United States Government nor any agency thereof, nor the Regents of the University of California, nor any of their employees, makes any warranty, express or implied, or assumes any legal responsibility for the accuracy, completeness, or usefulness of any information, apparatus, product, or process disclosed, or represents that its use would not infringe privately owned rights. Reference herein to any specific commercial product, process, or service by its trade name, trademark, manufacturer, or otherwise, does not necessarily constitute or imply its endorsement, recommendation, or favoring by the United States Government or any agency thereof, or the Regents of the University of California. The views and opinions of authors expressed herein do not necessarily state or reflect those of the United States Government or any agency thereof or the Regents of the University of California.

Research and Development

UCRL-16089

UNIVERSITY OF CALIFORNIA

Lawrence Radiation Laboratory
Berkeley, California

AEC Contract No. W-7405-eng-48

A MEASUREMENT OF THE POLARIZATION OF SIGMA-ZERO HYPERONS PRODUCED BY PI-MINUS MESONS ON HYDROGEN NEAR 1.3 BeV/c

Richard L. Crolius
(Ph.D. Thesis)

May 26, 1965

A MEASUREMENT OF THE POLARIZATION OF SIGMA-ZERO HYPERONS PRODUCED BY PI-MINUS MESONS ON HYDROGEN NEAR 1.3 BeV/c

Contents

Abstract v

I. Introduction

A. Purpose of Experiment 1

B. Polarization Theory 2

C. $\Sigma\Lambda$ Parity Theory 3

II. Experimental Apparatus and Method

A. Overall Description of the Experiment 7

B. Beam Design 7

C. Experimental Apparatus 11

D. Electronics 18

E. Optics and Camera 19

III. Data Analysis

A. Scanning 26

B. Measuring 27

C. Selection of Events 31

D. Analysis of Selected Events 35

IV. Results

A. Cross Sections; Adder Efficiency 37

B. Polarization 44

C. Discussion of Results 44

V. Conclusions 47

Acknowledgments 49

Appendix - Calculation of the Number of Dalitz Decays Required to Measure the $\Sigma\Lambda$ Parity 50

References 52

A MEASUREMENT OF THE POLARIZATION OF SIGMA-ZERO HYPERONS PRODUCED BY PI-MINUS MESONS ON HYDROGEN NEAR 1.3 BeV/c

Richard L. Crolius

Lawrence Radiation Laboratory
University of California
Berkeley, California

May 26, 1965

ABSTRACT

Spark chambers were used to detect $\Sigma^0 + K^0$ production by π^- mesons on hydrogen in the π^- momentum range 1200 to 1400 MeV/c. Differential cross-section measurements are presented. The differential cross sections remain unchanged, within the limits of statistics, from 1200 to 1400 MeV/c. A measurement of the Σ^0 polarization indicates that the polarization may be changing rapidly with beam momentum, but poor statistics prevent establishing this conclusively.

I. INTRODUCTION

A. Purpose of Experiment

The Σ^0 polarization experiment was conceived as a preliminary to another experiment – a measurement of the $\Sigma\Lambda$ relative parity, which requires polarized Σ^0's.

The Σ^0 polarization is obtained from a study of the most-common Σ^0 decay mode

$$\Sigma^0 \rightarrow \Lambda^0 + \gamma \,. \tag{1}$$

The $\Sigma\Lambda$ relative parity can be obtained from a study of the rarer Dalitz-pair decay mode (branching ratio ≈ 1:180) of the Σ^0

$$\Sigma^0 \rightarrow \Lambda^0 + (e^+ + e^-) \,. \tag{2}$$

Both of these measurements were to be attempted with the same experimental apparatus. Although the polarization data presented here indicate the presence of Σ^0 polarization, there are not enough events of type (2) to permit the parity determination.

The method of this experiment was to observe (in spark chambers) decays (1) and (2) of Σ^0's produced in the reaction

$$\pi^- + p \rightarrow \Sigma^0 + K^0$$

at π^- momentum near 1.3 BeV/c. These events were identified by their charged secondary products:

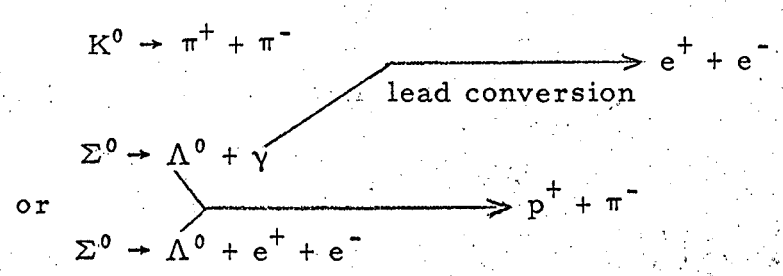

Such events are identified by two vees (Λ^0 and K^0 decays) and a pair of tracks emerging either from the lead (conversion pair), or the production vertex (Dalitz pair); they are then confirmed by kinematical analysis.

B. Polarization Theory

Consider first the most-common decay mode

$$\Sigma^0 \rightarrow \Lambda^0 + \gamma \ . \tag{1}$$

This is a parity-conserving electromagnetic transition. Because the Σ^0's are produced in the parity-conserving strong interaction

$$\pi^- + p \rightarrow \Sigma^0 + K^0 \ , \tag{3}$$

any Σ^0 polarization, $\vec{P}_\Sigma$, must be in the direction $\hat{N} \propto \vec{k}_\pi \times \vec{k}_\Sigma$, i.e., normal to the Σ^0 K^0 production plane. The angular momentum of the photon must be along its direction of motion, so angular-momentum conservation will cause the Λ polarization to be in directions other than $\vec{P}_\Sigma$. It is therefore convenient for the density-matrix formalism to be employed, whereby polarization in an arbitrary direction may be represented as an expansion in eigenstates of S_Z.

The sigma state can be represented by a spinor χ_Σ for which the density matrix is

$$\rho_\Sigma = \chi_\Sigma \chi_\Sigma^\dagger = \frac{1}{2}(1 + \vec{P}_\Sigma \cdot \vec{\sigma}) \ . \tag{4}$$

The lambda is represented by a spinor $\chi_\Lambda = T\chi_\Sigma$, where T is the transition matrix for this decay (1), and the density matrix for the lambda is

$$\rho_\Lambda = \chi_\Lambda \chi_\Lambda^\dagger = T\,\chi_\Sigma \chi_\Sigma^\dagger\, T^\dagger = T\,\rho_\Sigma\, T^\dagger \ . \tag{5}$$

The lambda polarization is

$$\vec{P}_\Lambda = \mathrm{Tr}(\rho_\Lambda \vec{\sigma}) = \mathrm{Tr}(T\rho_\Sigma T^\dagger \vec{\sigma}) \ , \tag{6}$$

where Tr means trace.

To find the form of the transition operator T note that it must be scalar for even $\Sigma\Lambda$ parity and pseudoscalar for odd $\Sigma\Lambda$ parity. In the rest frame of the Σ the available vectors are $\hat{k}$, the direction of the decay γ, and $\hat{e}$, where $\hat{e}$ is the photon electric or polarization vector, and the pseudovectors are $\vec{P}_\Sigma$ and $\hat{n} = \hat{k} \times \hat{e}$. With the requirement that T be linear in $\hat{e}$ (the vector potential $\vec{A}$ is linear in $\hat{e}$, and the interaction Hamiltonian is linear in $\vec{A}$) the only forms possible are

$$T \propto \vec{\sigma} \cdot (\hat{k} \times \hat{e}) = \vec{\sigma} \cdot \hat{n} \quad \text{even parity (T scalar)} \tag{7}$$

$$T \propto \vec{\sigma} \cdot \hat{e} \quad \text{odd parity (T pseudoscalar).} \tag{8}$$

Therefore by (6)

$$\langle \vec{P}_\Lambda \rangle = \mathrm{Tr} \left\{ \vec{\sigma} \cdot (\hat{k} \times \hat{e}) \left[\frac{1}{2} (1 + \vec{P}_\Sigma \cdot \vec{\sigma}) \right] \vec{\sigma} \cdot (\hat{k} \times \hat{e}) \, \vec{\sigma} \right\} \quad \text{even parity}$$

$$\langle \vec{P}_\Lambda \rangle = \mathrm{Tr} \left\{ \vec{\sigma} \cdot \hat{e} \left[\frac{1}{2} (1 + \vec{P}_\Sigma \cdot \vec{\sigma}) \right] \vec{\sigma} \cdot \hat{e} \, \vec{\sigma} \right\} \quad \text{odd parity.}$$

Evaluating these expressions is straightforward and gives

$$\langle \vec{P}_\Lambda \rangle = -\vec{P}_\Sigma + 2 (\vec{P}_\Sigma \cdot \hat{n}) \hat{n} \quad \text{even} \tag{9}$$

$$\langle \vec{P}_\Lambda \rangle = -\vec{P}_\Sigma + 2 (\vec{P}_\Sigma \cdot \hat{e}) \hat{e} \quad \text{odd.} \tag{10}$$

Because the photon polarization is practically unmeasurable, $\hat{e}$ and $\hat{n} = \hat{k} \times \hat{e}$ are unknown. Averaging either (9) or (10) over all possible directions of $\hat{e}$ gives[1]

$$\overline{\langle \vec{P}_\Lambda \rangle} = -(\vec{P}_\Sigma \cdot \hat{k}) \hat{k} \, . \tag{11}$$

The Σ^0 polarization was calculated by means of this expression*, the Λ polarization being measurable from the asymmetric distribution, I_π, of pions in Λ decay:

$$I_\pi(\cos\theta) = \frac{1}{2} \left[1 + a_\Lambda (\vec{P}_\Lambda \cdot \hat{k}_\pi) \right], \tag{12}$$

where $\cos\theta = \hat{P}_\Lambda \cdot \hat{k}_\pi$. Here k_π is the direction of the decay pion in $\Lambda^0 \to p + \pi^-$. Thus the sigma polarization is obtainable from measurements of $\hat{N}$, $\hat{k}$, and $\hat{k}_\pi$ for a sufficiently large set of events.

C. $\Sigma\Lambda$ Parity Theory

In Eqs. (9) and (10) we saw that for decay (1) the lambda polarization (which is measurable) is correlated with the photon polarization (which is not measurable) in a way that depends on the $\Sigma\Lambda$ relative parity. Several authors have shown that, in Dalitz decays of the Σ^0,

---

*The well-known relation $\vec{P}_\Lambda = -1/3 \, \vec{P}_\Sigma$ is obtained by averaging (11) over all possible directions of $\hat{k}$.

"memory" of the photon polarization is retained in the relative orientation and momenta of the pair.[2,3] The calculation is complicated because the pair is produced by a virtual photon that has longitudinal components and nonzero mass.

In order to see the analogy between the photon and Dalitz-pair parameters consider the schematic diagrams of Fig. 1.

For the case where $|\vec{k}(e^+)| = |\vec{k}(e^-)|$, Sucher and Snow[4] found expressions like (9) and (10):

$$\langle \vec{P}_\Lambda \rangle = -\vec{P}_\Sigma + 2(\vec{P}_\Sigma \cdot \hat{q})\hat{q} \qquad \text{even } \Sigma\Lambda \text{ parity} \qquad (13)$$

$$\langle \vec{P}_\Lambda \rangle = -\vec{P}_\Sigma + 2(\vec{P}_\Sigma \cdot \hat{n})\hat{n} \qquad \text{odd } \Sigma\Lambda \text{ parity,} \qquad (14)$$

where

$$\hat{k} \propto \vec{k}(e^+) + \vec{k}(e^-);$$

$$\hat{q} \propto \vec{k}(e^+) - \vec{k}(e^-);$$

and

$$\hat{n} \propto \hat{k} \times \hat{q}\,.$$

The vector $\hat{q}$ is in the direction of the electric field between the electrons and is analogous to $\hat{e}$ in Eq. (8); thus the $\hat{n}$'s are comparable. The two parity cases are switched because the fermion-antifermion pair produced is pseudoscalar. When $\vec{P}_\Lambda$ is averaged over the invariant-mass distribution of the pair, the result is[5,6]

$$\langle \vec{P}_\Lambda \rangle = -\hat{k}(\vec{P}_\Sigma \cdot k) \mp 0.43 \left[\hat{n}(\vec{P}_\Sigma \cdot \hat{n}) - \hat{m}(\vec{P}_\Sigma \cdot \hat{m})\right]^{\text{even}}_{\text{odd}}\,. \qquad (15)$$

For this general case of unequal electron momenta, $\hat{q}$ is no longer perpendicular to $\hat{k}$ as in (13) and has been replaced by $\hat{m} = \hat{k} \times \hat{n}$. This is the expression required for the $\Sigma\Lambda$ parity to be measured by our spark-chamber technique because it requires no momentum measurement of the electrons. Notice that one need not even know which is the electron and which the positron, because $\langle \vec{P}_\Lambda \rangle$ is bilinear in $\hat{m}$ and $\hat{n}$. A calculation of the number of Dalitz-decay events required for the parity to be measured by this method is presented in Appendix A.

Since this experiment was performed, a $\Sigma\Lambda$ parity measurement has been reported by Courant et al.,[7] who used the Dalitz-pair invariant-mass distribution from Σ^0's produced by K^- mesons stopping in the CERN 80-cm hydrogen bubble chamber rather than the angular-correlation method discussed here.

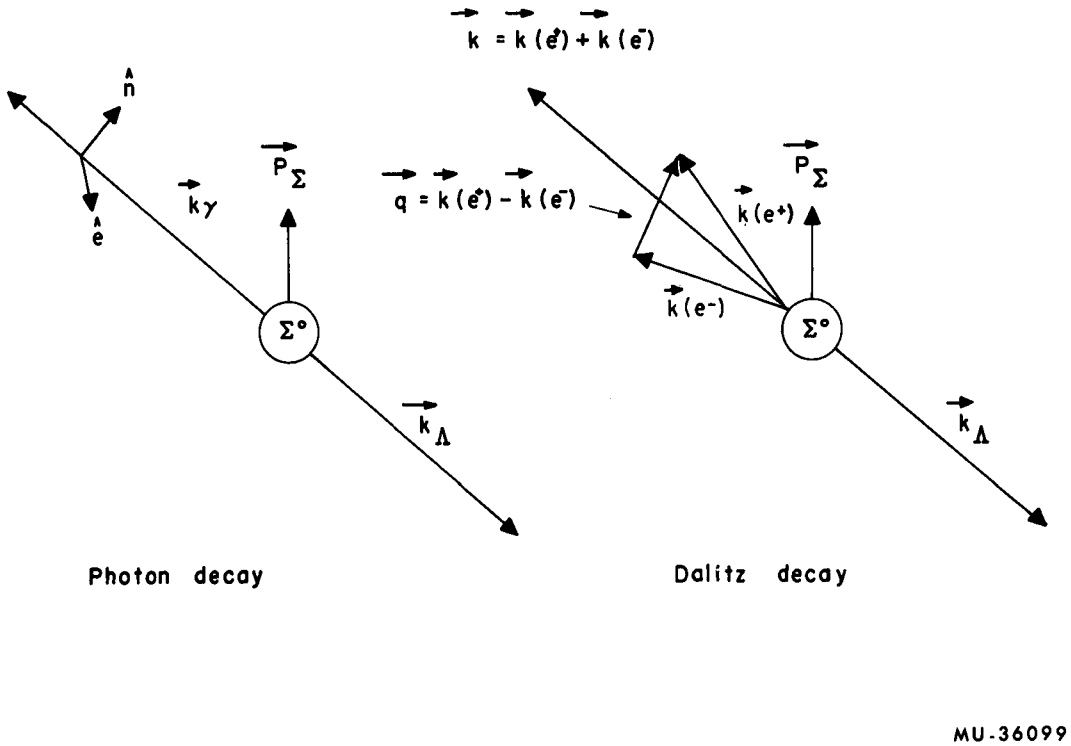

Fig. 1. Diagram showing Σ^0 decay and parameters.

Although the two methods depend upon the same calculational approach, the invariant-mass distribution relies on detailed assumptions concerning the electric form factors. Since the correlation method is free from such assumptions, it provides an independent check of the CERN result. The analyzing coefficient 0.43 in Eq. (15) is actually an average over the invariant-mass distribution of the pair. For any particular invariant mass, it is[5]

$$(1 - 4\, m_e^{\,2}/k_\mu^{\,2})/(2 + 4\, m_e^{\,2}/k_\mu^{\,2}) < 0.5,$$

where k_μ is the invariant mass and m_e the electron mass. In principle k_μ can be measured for each event, but in any case it is clear that the method is insensitive to the distribution of k_μ. Moreover the experiment of Courant et al. has established the distribution of k_μ.

II. EXPERIMENTAL APPARATUS AND METHOD

A. Overall Description of the Experiment

The experimental technique was to photograph secondary products of the reaction

$$\pi^- + p \rightarrow \Sigma^0 + K^0$$

in spark chambers. A beam of π^- mesons from the Bevatron passed down the beam channel (Fig. 2) and entered the experimental apparatus (Fig. 3). The beam interacted with protons in the liquid-hydrogen target and secondary particles passed through the semi-cylindrical spark chambers and were counted by the array of scintillation counters. When signals from the detecting counters satisfied the electronic logic (Fig. 4), a high-voltage pulse was applied to the spark chambers and the resulting spark tracks were photographed.

B. Beam Design

The beam optics were designed to maximize flux in a narrow momentum region while confining the beam at the hydrogen target to a region 1 in. high by 5 in. wide. Also considered were the advantages of placing the high-pressure Čerenkov counter at a focus and the need for an analyzing magnet just upstream of the experiment to permit a beam momentum measurement of each photographed event.

The π^- beam originated from a 2-in. diam copper target flipped into the 6-BeV circulating proton beam of the Bevatron just upstream of the west straight section. Negative particles produced at 0° entered the beam channel at the beam window, Fig. 2.

The principal lens elements were an 8-in. quadrupole doublet, Q_1, placed as close as possible to the Bevatron to maximize angular acceptance, and a similar doublet, Q_4, which refocussed the beam onto the hydrogen target. Two 8-in. quadrupole doublets Q_2 and Q_3, constituting a field lens, were placed on either side of the gas Čerenkov counter (at the focus of Q_1) to minimize dispersion losses.

Momentum selection was provided by 8-by-16-in. aperture bending magnets M_1 and M_2 near Q_1 and Q_4 respectively; M_2 was placed just upstream of the experimental apparatus.

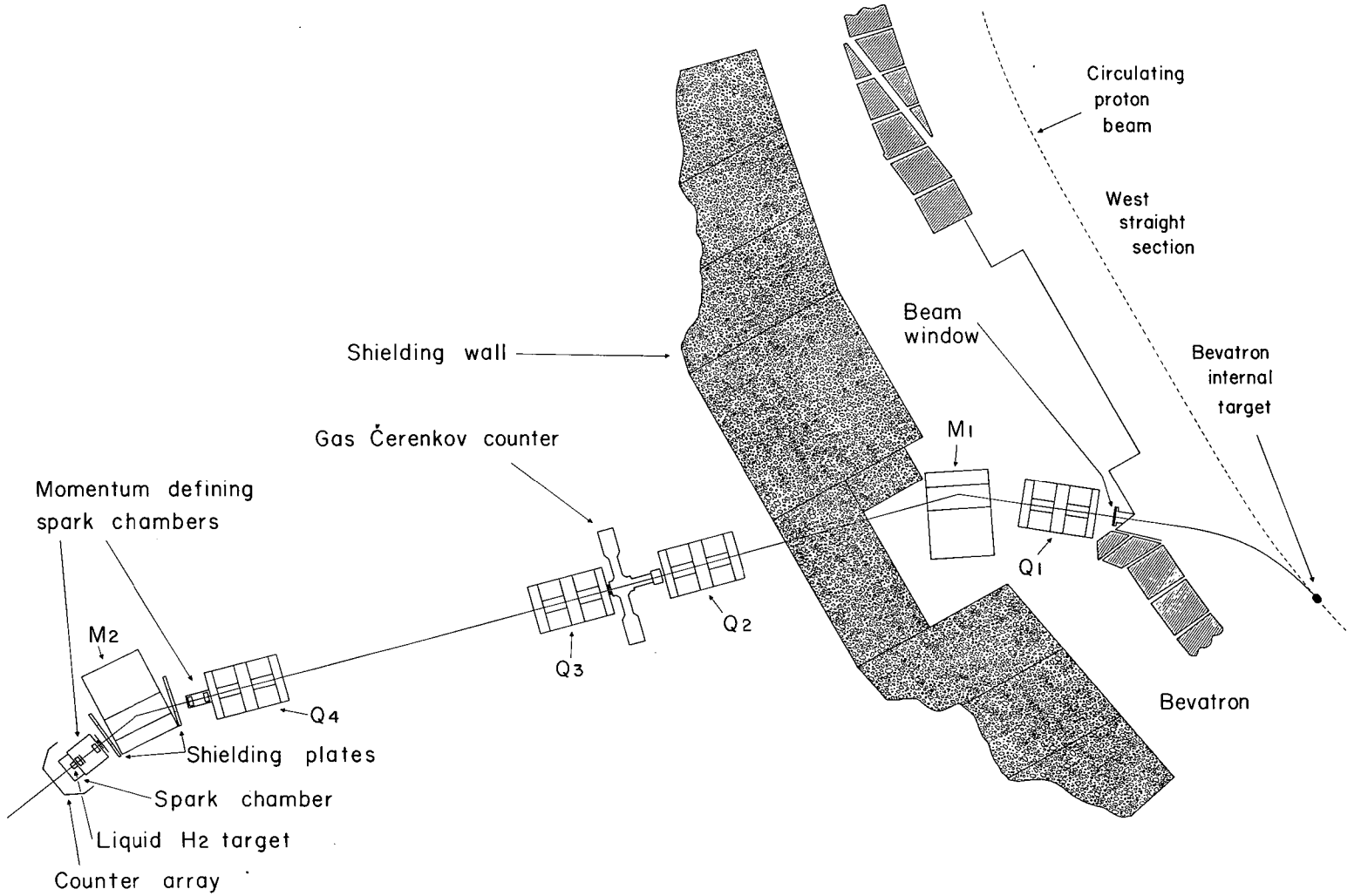

Fig. 2. Pion-beam layout.

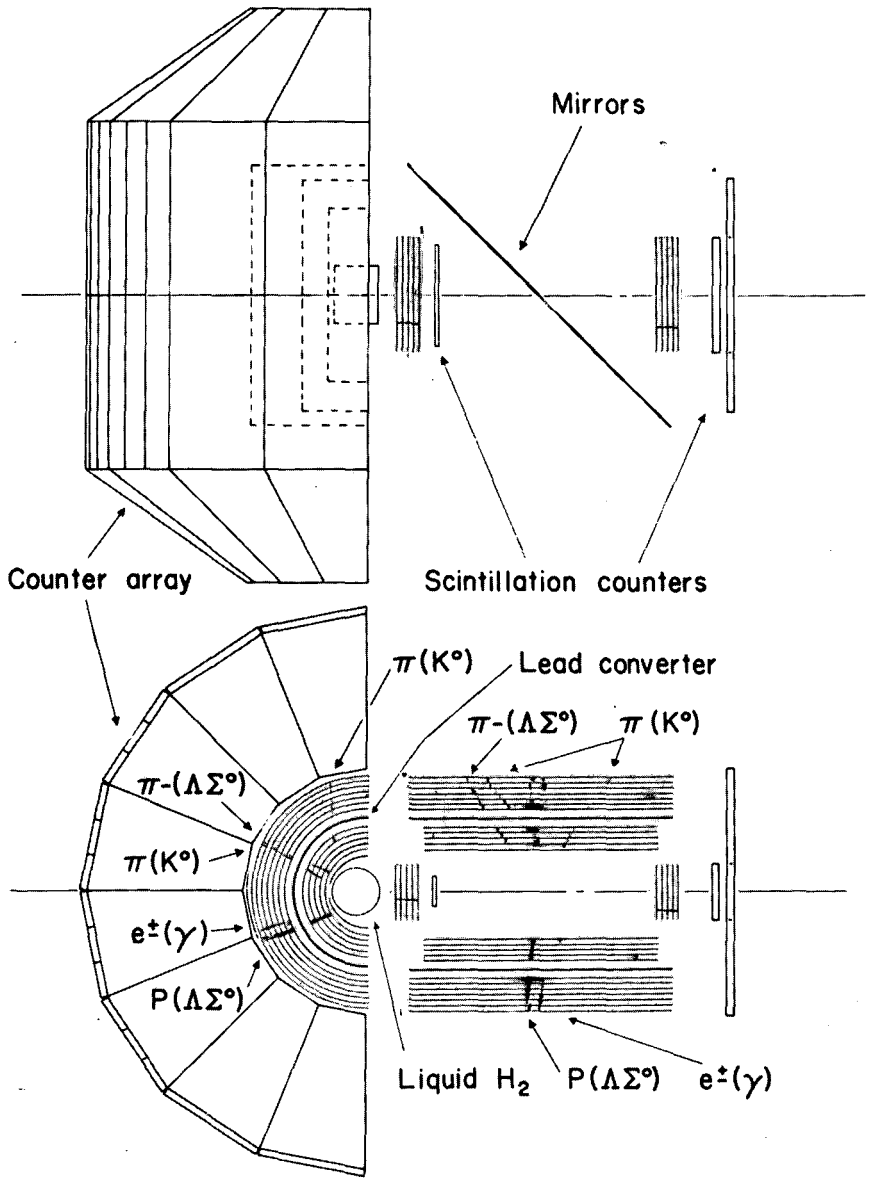

ZN-5009

Fig. 3. Experimental arrangement with a photograph of an event superimposed.

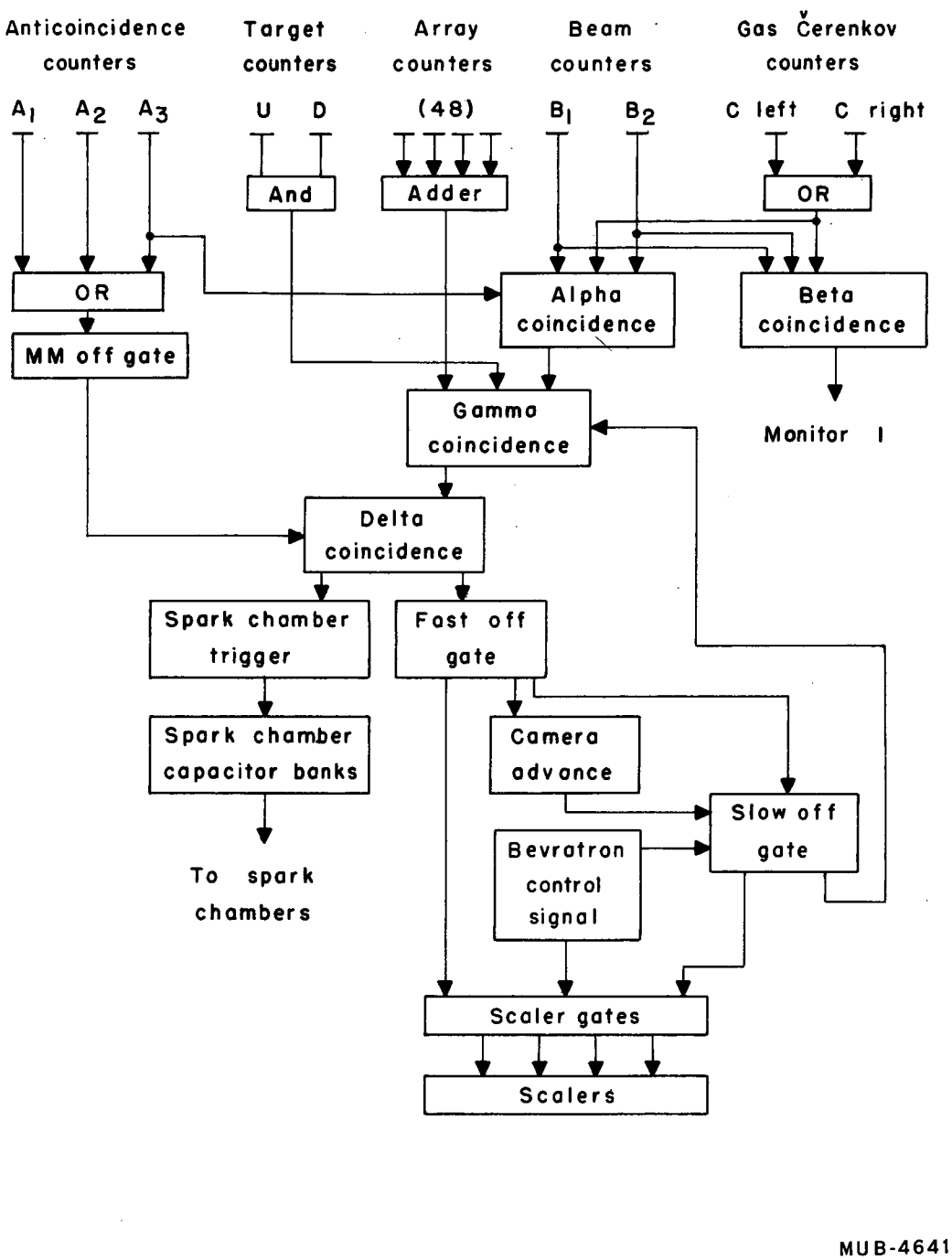

Fig. 4. Electronics block diagram.

The geometry of the liquid hydrogen target (allowed beam area 1 inch high by 5 inch wide) allowed considerable horizontal dispersion caused by the Bevatron's magnetic field.

Helium was maintained at atmospheric pressure along the beam channel to minimize Coulomb scattering.

C. Experimental Apparatus

1. General Picture

The liquid-hydrogen target and detecting apparatus are shown in Figures 3 and 5. Beam particles passed through a channel in fiducial box G [Fig. 5(a) and (b)] where they were seen in beam chambers BC, and interacted in the liquid-hydrogen target F. Mirrors BM show the 90° stereo view of the beam tracks. Charged secondary reaction products passed through the semicylindrical spark chambers (which were normally behind field lens L) and were seen as spark tracks. Mirrors S provide a 90° stereo view of the tracks; the spark light is reflected around the gaps by the hand-polished plates. A photograph of a typical event in these chambers was superimposed on Figure 3, and a full frame is shown in Figure 6.

The 48-member array of scintillation counters detected charged particles. If a given minimum number (usually set at 5) counted with a coincident beam track, the electronic logic produced a high-voltage pulse to trigger the spark chambers.

2. Target

The chief design consideration for the target was the need to minimize the mass to be traversed by both the beam and secondary particles. Because high multiplicity of secondaries was used as the triggering criterion, it was important to minimize construction materials in the beam to reduce high-multiplicity stars caused particularly by interactions of the beam with heavy nuclei.

In addition there was the requirement of minimizing construction materials in all directions within the solid angle of detection. The parity measurement requires establishing the orientation of the plane of the Dalitz pair. Because the mean opening angle of the pair is $\approx 6°$, the allowed Coulomb scattering per electron is about 3°. Thus the target was made small and thin-walled to reduce multiple scattering and gamma

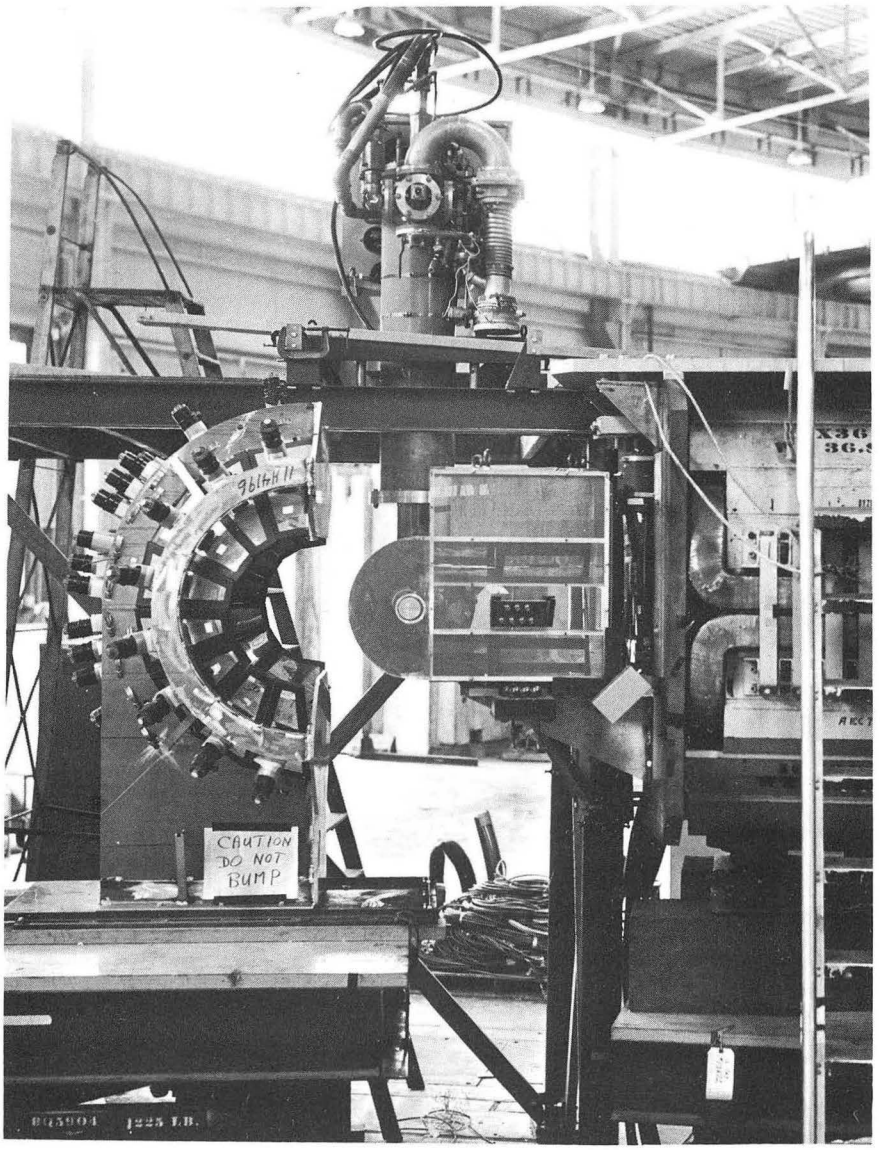

ZN-5005

Fig. 5(a). Experimental apparatus. Counter array has been pulled back from target and the spark chambers removed.

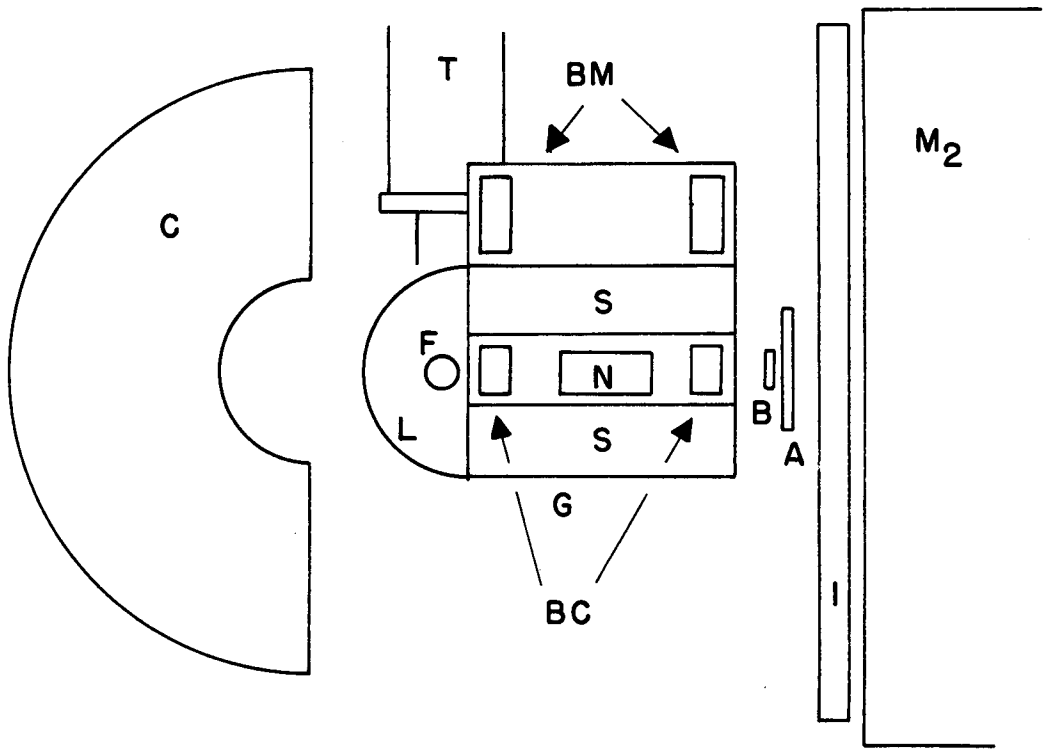

A. Anti counter, A_1

B. Beam counter, B_2

BC. Beam chambers

BM. Mirrors for stereo view of beam chambers

C. 48 counter array

F. LH_2 target

G. Fiducial box

L. Field lens projecting over cylindrical chamber position

M_2. Bending magnet, M_2

N. Nixie lights

S. Locations of stereo mirrors

I. Iron shielding plate

MUB-5632

Fig. 5(b). Diagram of Fig. 5a.

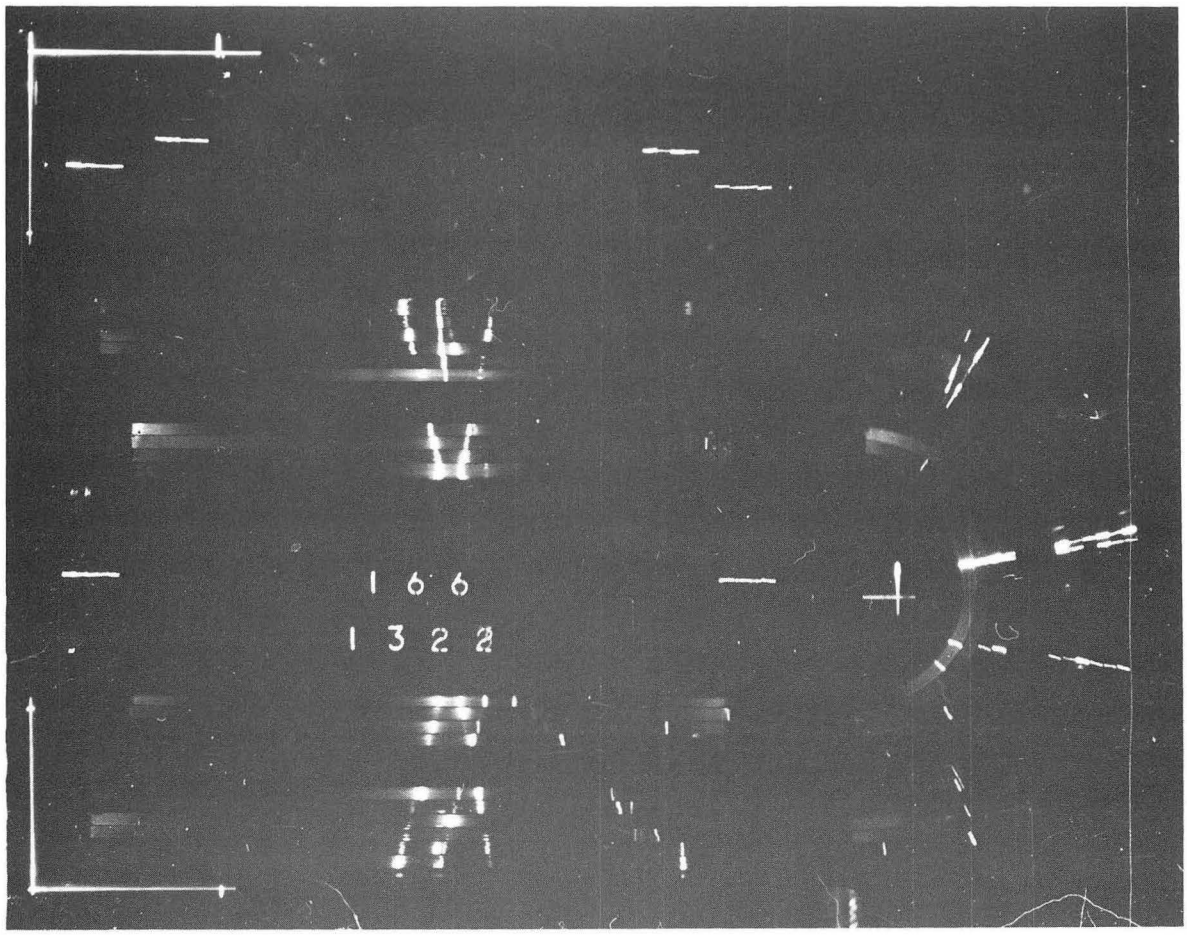

ZN-5033

Fig. 6. Photograph of an event.

conversions; it was made small also to make Λ^0 and K^0 vees visible in the chambers for easy identification, but scanning and resolution difficulties negated this advantage, as discussed in Sec. III.C.4. The flask was a cylindrical Mylar bag, 3 in. in diameter and 5 mils thick, supported by Lucite wedges in a 3.5 in. diam, 30-mil aluminum vacuum jacket that was evacuated below 0.02 micron.

3. Spark Chambers

Four parallel-plate spark chambers—one at each end of the fiducial boxes upstream and downstream of M_2—defined the incoming beam and permitted determination of the momentum of each photographed beam track to better than 1%. Each beam chamber had four 3/8-in. gaps. Iron plates 1-1/2-in. thick at the apertures of M_2 shielded the beam chambers from stray magnetic field.

The concentric semicylindrical chambers, Fig. 3, comprised the primary detection device. Figure 7 is a photograph of the outer chamber. The chief design consideration that led to the unusual cylindrical geometry was the desire to maximize the solid angle of detection.

The inner spark chamber had four 3/8-in. gaps; the outer had six. The plates were polished aluminum foil 3 mils thick cemented into slots in the 7/8-in. - thick Lucite end and side pieces. Ninety-degree stereo viewing was provided by two 45° mirrors. To help differentiate similar tracks in the mirror view, optical baffles were placed radially, one in each gap, at different azimuths. These baffles proved to be unnecessary, however, because the tracks were distinguishable by variable spark densities and clarity differences caused by attenuation on multiple reflections around the cylindrical gaps. For rigidity and protection from mechanical damage, the chambers were covered with 30-mil aluminum plates with windows of 2-mil aluminum foil in the beam channel.

Between the inner and outer chambers the chamber-support frame had slots to hold a removable plate of lead, (semicylindrical, 1/16-in. thick) which had a window to pass the incident π^- beam. The purpose of the lead was to convert gamma rays from the decays $\Sigma^0 \rightarrow \Lambda^0 + \gamma$.

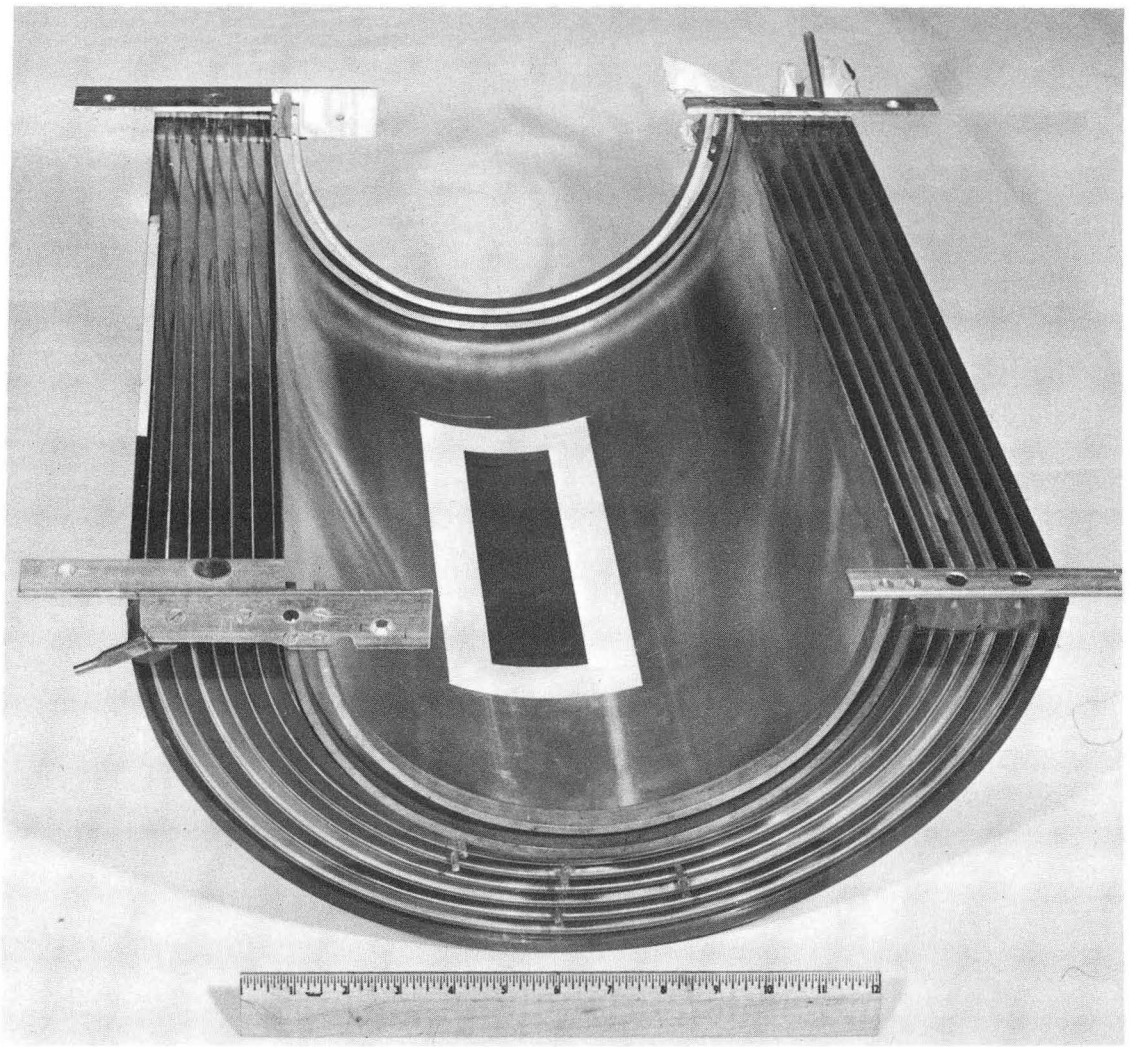

ZN-5007

Fig. 7. Outer semicylindrical spark chamber.

The gas was a commercial mixture of 10% helium and 90% neon.

4. Fiducial Boxes

The fiducial boxes (the downstream box can be seen in Fig. 5) were rigid structures of 1/2 in. aluminum and 1/2 in. Lucite that secured a convenient and firmly fixed optical system. Shelves supported the beam chambers and machined slots held the stereo mirrors. The downstream box contained beam-coincidence and anticoincidence counters; holes were cut in it to pass the incident beam and others were cut between the beam chambers and their stereo mirrors.

5. Momentum Determination

The momentum of each photographed beam track was determined from the bending angle in M_2 as shown in the mirror views of the upstream and downstream beam chambers. Wire orbits were photographed in the actual setup to establish the bending angle-momentum relationship. In this way the momentum of each event is measurable to better than 1%, being limited by the precision of the beam track measurements.

6. Triggering System

To trigger the high-voltage pulse to the spark chambers, the electronic logic, Fig. 4, required a coincidence between the beam coincidence, alpha, and the array, ("Adder", in Fig. 4), and sometimes U and D as explained below.

The array consisted of 48 scintillation counters 3/8-in. -thick, which densely surrounded the semicylindrical chambers. They were varied in size approximately inversely as the expected local flux of particles to minimize events lost by more than one particle going through the same counter.

The beam counters were: 8-by-4-by-1/4-in. scintillators B_1 and B_2; 1-in. -thick anticoincidence counter A_1; and gas Čerenkov counter $\check{C}$ having left and right channels C_L and C_R. The beam coincidence (alpha) required B_1, B_2, no A_1, and C_L or C_R. Photomultiplier tubes (RCA 6810A) were the light-detection elements in all counters.

The high-pressure gas Čerenkov counter ($\check{C}$) holding 450 psi nitrogen discriminated against K^-, $\bar{p}$, and other slow background. Other anti-counters, tried and rejected, included A_2, just ahead of the target; A_3 in the beam at the

array; and water Čerenkov counters in the beam 10 ft downstream of the array. Counter A_2 was discarded in an effort to save events with a backward pi from the K^0 decay; these events later proved to be unresolvable. Counter A_3 was discarded because it interfered excessively with the beam. The water counters were removed because they increased the trigger time and did not reduce the trigger rate.

When it was seen during the experiment that data accumulated too slowly to permit separate polarization and parity measurements, counters U and D were installed around the target in trigger coincidence. Their purpose was to enhance the ratio of Dalitz pair to gamma decays detected while permitting higher beam rates by reducing the background by means of the more stringent triggering requirement; the enhancement results from the fact that Dalitz electrons are counted in U and D, whereas gamma-rays are not. It was hoped that, by concentrating on one momentum for which there was evidence of polarization (1325 MeV/c), a simultaneous polarization and parity measurement could be done.

D. Electronics

1. Logic

On the electronics block diagram (Fig. 4), the spark chamber trigger is shown to require B_1, B_2, C_L or C_R, no anticounters, and the adder output produced by five or more array counters; target counters U and D were required during part of the running.

The trigger was initiated by gamma coincidence, which also triggered the Fast Off Gate, which

a. Initiated the camera advance mechanism;
b. Turned off several scalar gates;
c. Triggered the Slow Off Gate, which turned off gamma and several scalar gates until the camera was fully advanced to the next frame, whereupon the Camera-Advance reactivated the Slow-Off Gate.

2. Adder

The heart of the triggering system was a 50-channel adder-discriminator which limited, added, and discriminated the sum of output pulses from the 48 array counters. It was set to require five or more input pulses.

The schematic of this unit is shown in Fig. 8. Its response curve is shown in Fig. 9, which illustrates its ability to count high-multiplicity pulses accurately.

3. Spark-Gap Capacitor Bank

Obtaining high-multiplicity spark tracks of good quality (four to six particles per chamber) requires high-energy low-rise-time high-voltage pulses to the spark chambers.

A 15-kV low-inductance capacitor bank of three spark gaps triggered the spark chambers. Figures 10 and 11 are a photograph of the bank, and a circuit diagram for one gap, respectively. Each gap controlled three decoupled banks of up to ten 4000-pF 30-kV barium titanate capacitors (Sprague No. 6134). The capacitors were mounted on copper sheets, the high-voltage sheets running only 1/8 in. from the ground sheets to minimize inductance. Each 40 000-pF bank fed six 50-ohm coaxial output cables. For this experiment the banks were run at partial capacity, with 40 000 pF for the 10 000 pF cylindrical spark chambers, and 3000 pF for each of the 750-pF beam chambers. The banks supplied 15-kV negative pulses. A spark-chamber clearing field of + 22 V was used. Gap efficiency varied from about 98% with one track in the chambers to 70% with six tracks in the chambers.

E. Optics and Camera

1. Layout

The layout of the camera, mirrors, and chambers is shown in Fig. 12. The camera views the experiment at A through mirror N. A small mirror S, attached to N, superimposes the plan view of the upstream beam chambers onto the picture. A complete frame of an actual event is shown in Fig. 6.

A 5-ft diameter plano-convex field lens of 30-ft focal length was machined from Lucite, polished, and cut to fit over the downstream fiducial box and semicylindrical chambers.

2. Alignment Procedure

The system was designed to be rigid to minimize alignment problems. The fiducial boxes were of rigid structure and were hung

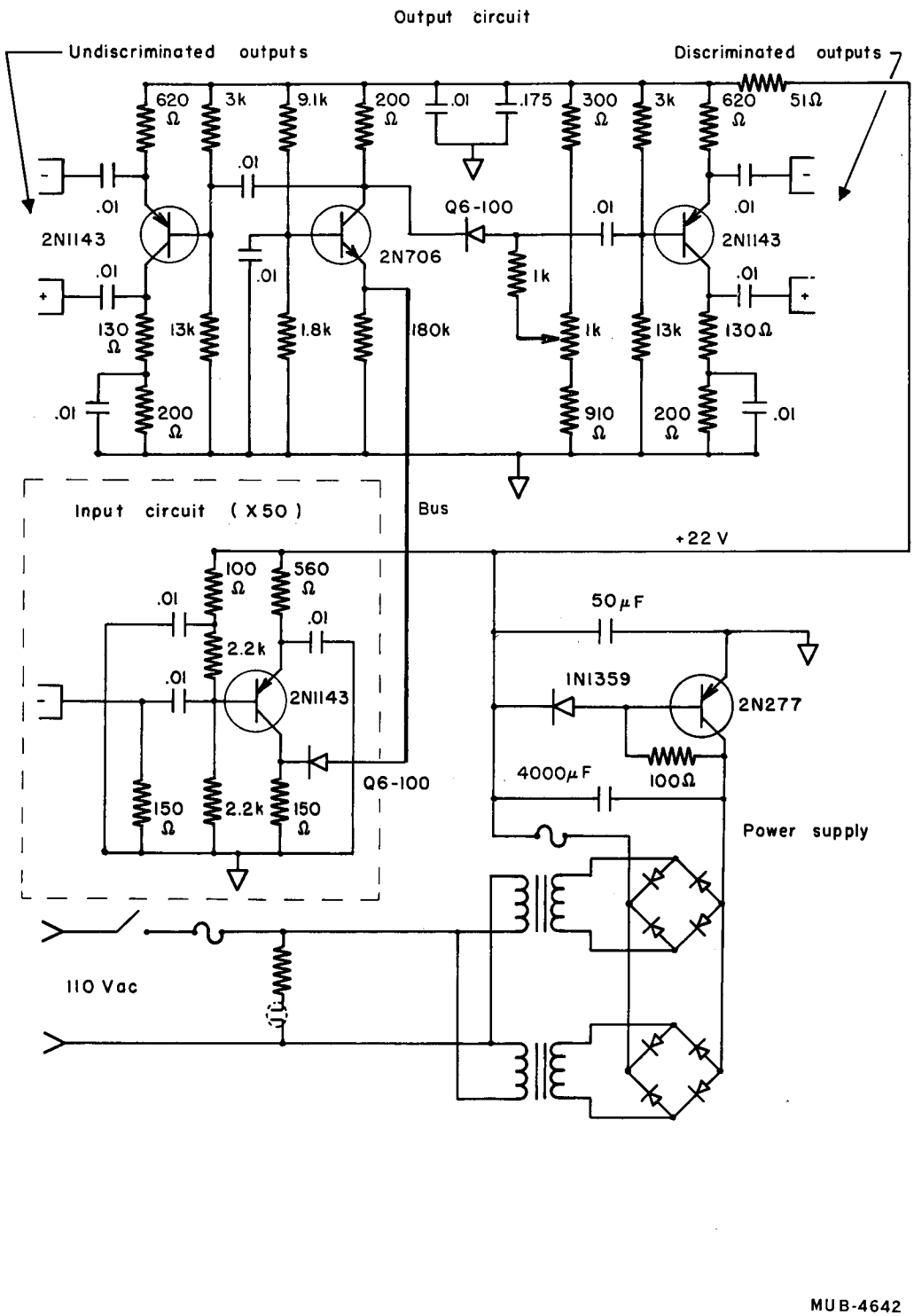

Fig. 8. Circuit diagram of adder-discriminator. Capacitances are given in microfarads.

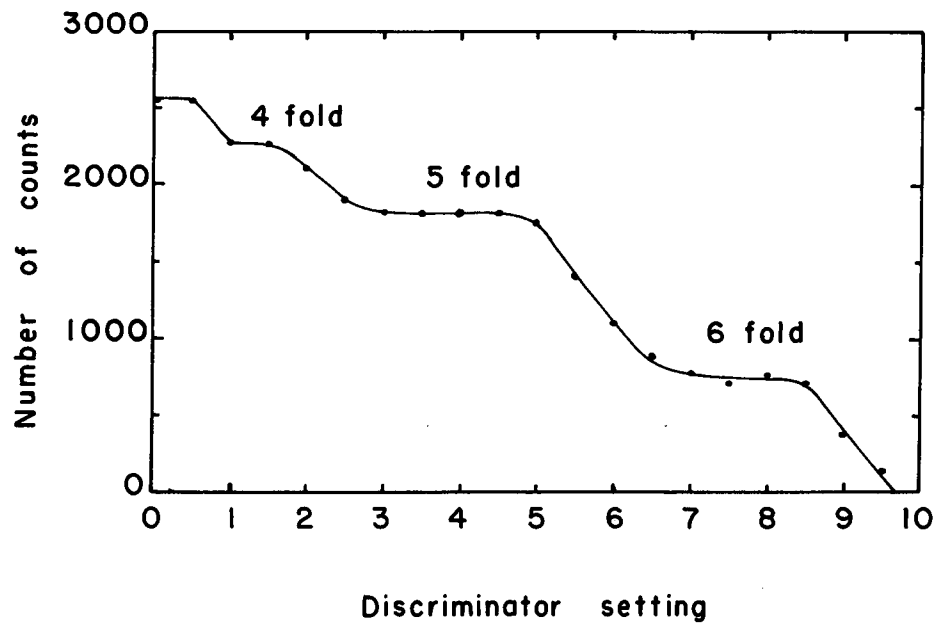

MU-36100

Fig. 9. Adder resolution for high-multiplicity inputs. Counting rate of discriminated output pulses is plotted against discriminator setting. The existence of plateaus demonstrates the discrete levels of pulse height.

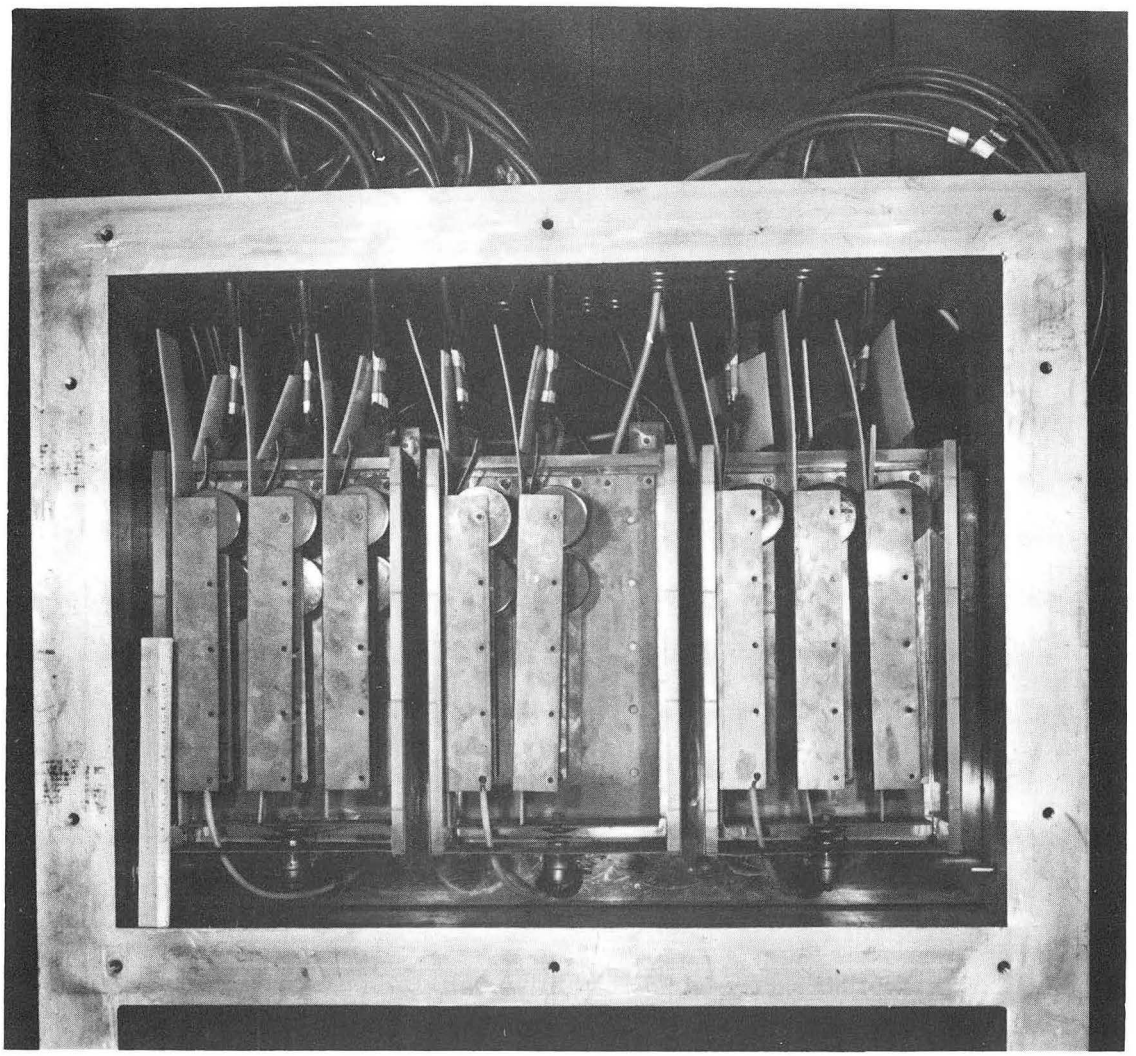

ZN-5006

Fig. 10. Photograph of three-spark-gap capacitor bank at partial capacity. A one-foot measuring stick is shown for size comparison.

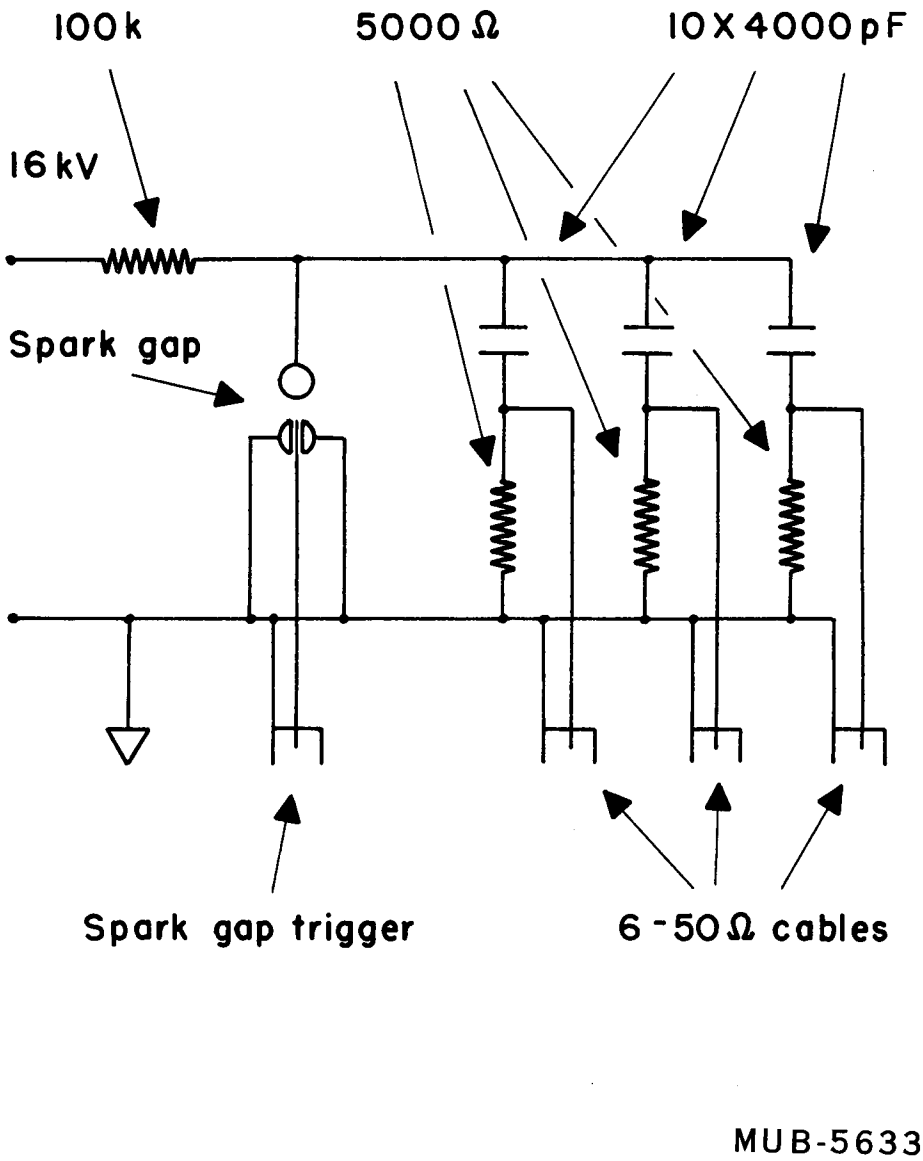

Fig. 11. Circuit diagram for one spark gap.

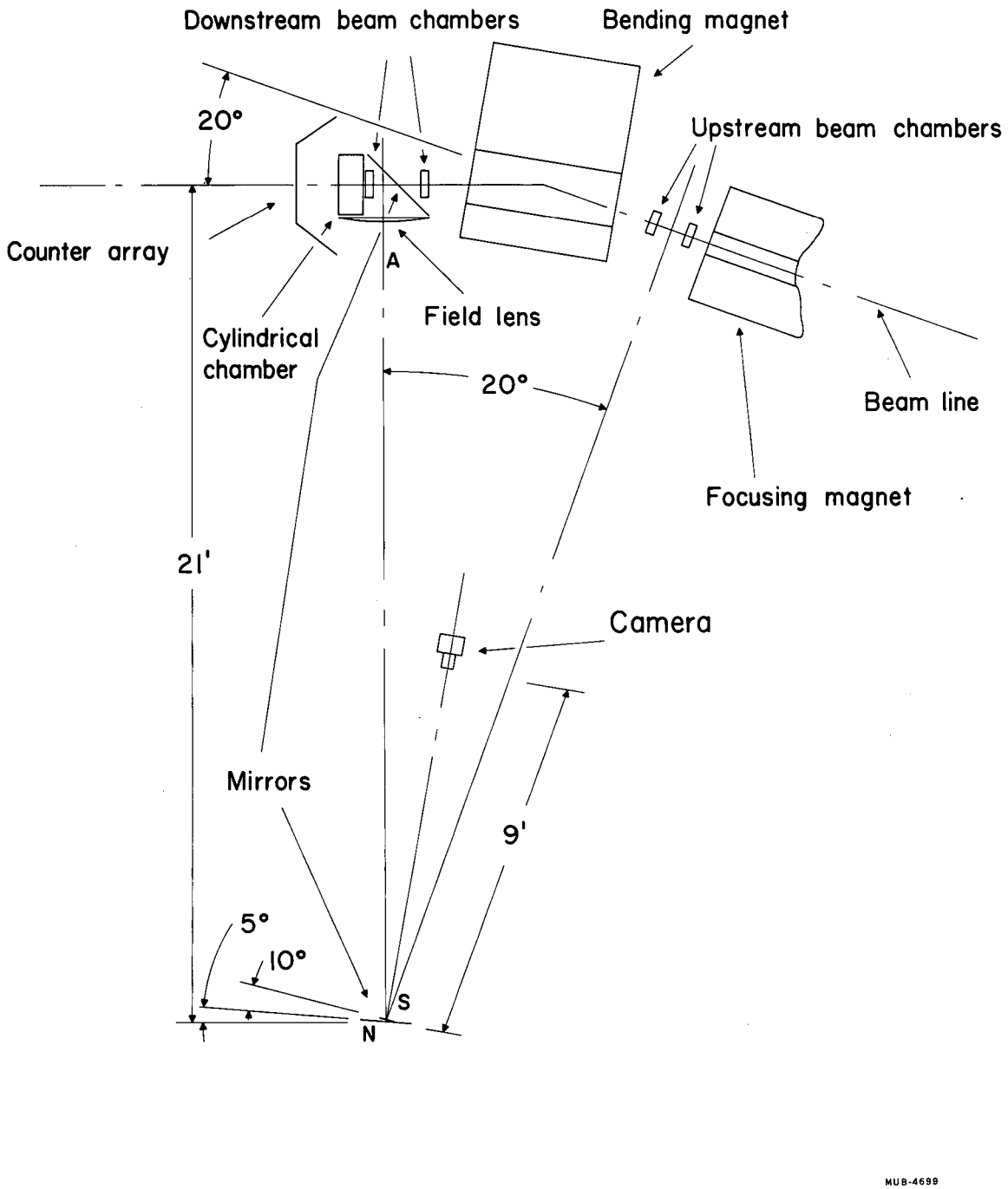

Fig. 12. Plan view of apparatus and optical arrangement.

from the ends of a 2-in. -thick aluminum plate bolted to the top of M_2. Final optical alignment was achieved by adjusting the fiducial boxes until, as seen through the camera, pre-etched fiducial marks on the fronts of the boxes were aligned with mates seen in the mirrors on the side surfaces.

3. Camera, Film, and Exposure Data

The camera was a modified Flight Research Model 4c. With a film-advance cycle time of 40 msec it was capable of taking as many as ten 35-mm frames during the 0.4-sec Bevatron beam spill time.

The experiment was light shielded and exposure was made with an open f/8 lens on Dupont 140B film with Microdol development. Brightness losses caused by mirror or plate reflections were compensated for by neutral density filters placed over the various views. The direct view of the semi-cylindrical chambers and the mirror views of the beam chambers were covered with 0.3 density filters (intensity factor of 2) and the direct views of the beam chambers were covered with 0.6 density filters (intensity factor of 4).

About 1.6 million events were photographed; the polarization measurement was made from about 300 $\Sigma^0 K^0$ events obtained from 1.2 million photographs taken with the lead converter in place.

III. DATA ANALYSIS

A. Scanning

1. General Discussion

The triggering background was so high (≈ 4000:1) that a large scanning effort was required. The measuring load was reduced by knowledgeable scanners who rejected, before measuring, events that appeared to be either kinematically or topologically impossible. As it turned out, about seven events were measured for each fit found. The solution adopted was prescanning of the film with simple qualitative selection rules and then second-scanning by another group of scanners armed with an understanding of the kinematical and geometrical criteria and of the cylindrical geometry.

2. Scanning Instructions

a. Prescanning. Prescanners selected events with four charged secondaries plus gamma-conversion products, i.e., tracks appearing only in the outer semicylindrical chamber and converging at the lead, which could therefore represent gamma-conversion electrons. The prescanners also used spark-counting criteria to reject events having multiple-beam or fragmentary tracks.

b. Second Scanning. Second scanners chose events to be measured from those events selected by the prescanners. They understood the production and decay processes, used kinematical cutoff rules, and also knew detailed construction techniques to establish the allowed range of apparent curvature of tracks in the cylindrical geometry, as discussed in Sec. III. A. 3. They rejected events whose four prongs intersected the incoming pion track within a 1/8-in. circle, events which clearly originated outside the target, and events for which it was not possible to make Λ^0 and K^0 vees.

3. Scanning Problems

It would be a simple matter to instruct scanners to look for vees were it not for the cylindrical geometry, which causes straight tracks to appear curved, in general, in the mirror view. Figure 13 illustrates the effect; it is a photograph of a beam track passing through the system, interacting with the cover of the chamber and sending backward a charged

secondary, whose path appears hyperbolic in the mirror view. The equation of a track as seen in the mirror is

$$R^2 - \frac{(Z - Z_0)^2}{\tan^2 \lambda} = b^2. \tag{16}$$

(The variables are shown in Fig. 14.) Evidently all tracks appear curved in the mirror except those which are radial ($b = 0$) and/or without dip ($Z \equiv Z_0$, $\lambda = 0$). In practice, tracks coming from the target region are nearly radial and appear straight.

Second scanners were taught constructions to establish limits on the curvature possible to a track inside the chambers in the region where the track is not seen; by means of these constructions, events that looked topologically impossible could frequently be rejected.

B. Measuring

1. SCAMP Measuring Devices

Events selected by second scanners were measured on SCAMP II and SCAMP III digitized measuring protractors. With these devices the measurer sees the event projected on a ground-glass screen. He controls a translating film stage and a rotating fiducial reticle; a single setting on a spark track records on magnetic tape the orientation of the track or fiducial line and the film coordinates of one point. Various constants and event codes were set on a parameter board.

2. Measuring Problems

a. Hyperbolic tracks. It was not necessary to fit a hyperbola to each cylindrical chamber track to solve the problem of curved tracks in the mirror view. It was sufficient only to measure three coordinates of two points on each track; on the SCAMP parameter board the measurer recorded the numbers of the spark-chamber plates that were at the ends of the segment of track he used for the measurement. In the track reconstruction program, the intersection of the track lines with the plate surfaces determined two sets of x, y, z coordinate points per track, and thus the question of track curvature was avoided.

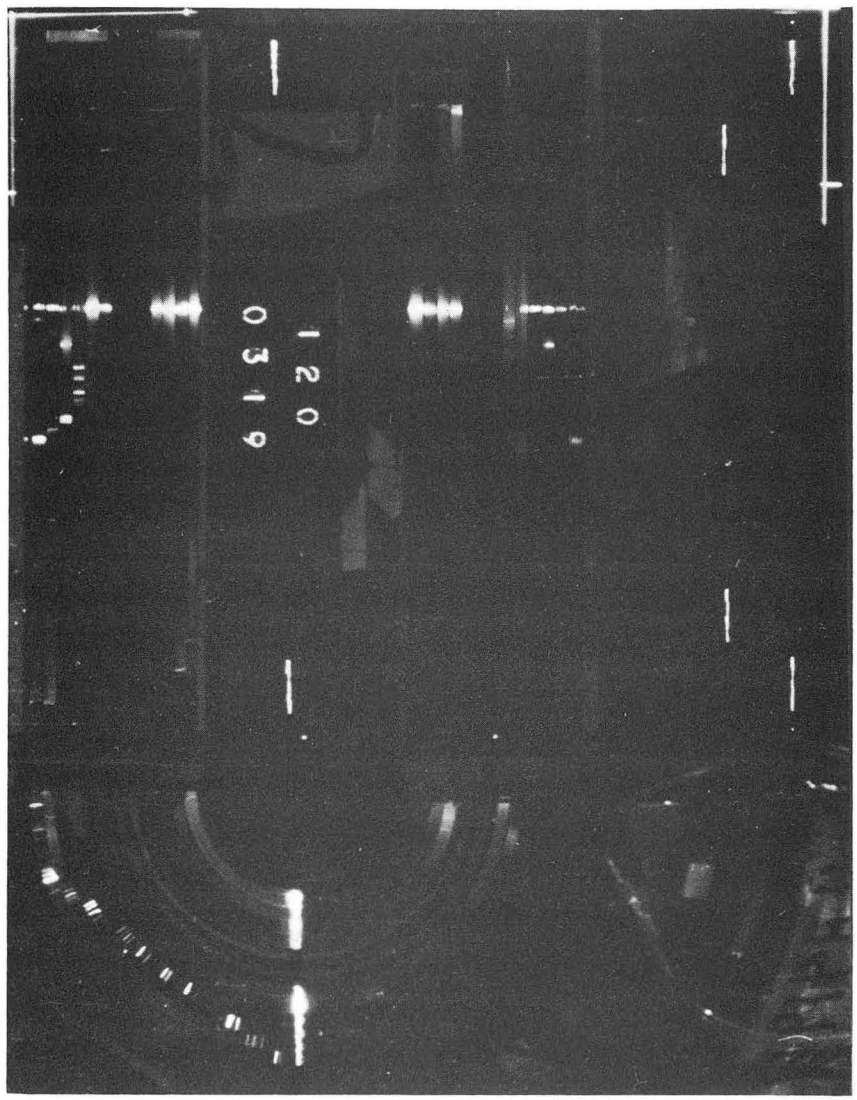

ZN-5008

Fig. 13. Photograph of hyperbolic track image.

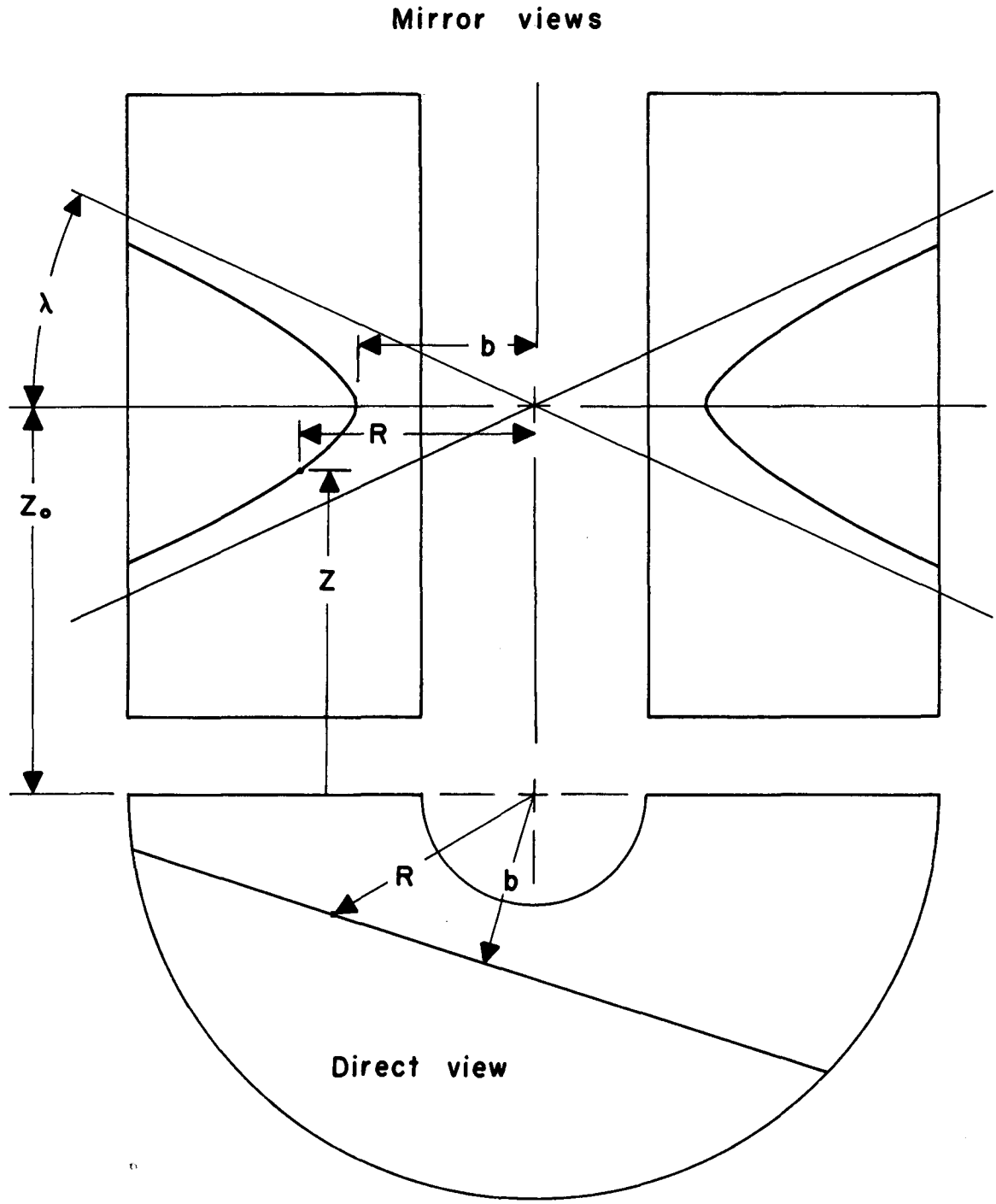

MUB-5742

Fig. 14. Distortion of a straight track by the cylindrical geometry. Lambda is the track's actual dip angle and apparent asymptotic dip angle.

b. Lead scatters. The scattering point of a track that scattered at the lead was used by the measurer to supplement the inner chamber sparks.

b. Hidden tracks. If the location of a track was ambiguous, e.g., if a track was hidden in one view by one of two other tracks, the measurer set on both of the possible locations; the fitting program analyzed the event separately for the two cases.

d. Poor tracks. Provision was made for tracks that were poorly determined because of broad sparks, faintness, or obscuration. The measurer set on such tracks twice, expressing limits on the possible positions. The settings were averaged and the measurements themselves were used as expressions of increased error to be assigned to the track.

e. Inner-plate effect. An interesting effect, which was not actually a problem, was seen in the cylindrical chambers. For track-to-plate normal angles greater than $\approx 30°$, the spark did not follow the particle path, but usually originated from the point where the particle path crossed the inner (smaller radius) of the two plates bounding the gap. This effect could be seen readily for any nonradial track by extrapolating the track in from the outer chamber, where it was more radial, to the inner chamber. The regularity of the effect probably improved the accuracy of track measurements, but is not easily understood. The only explanation that offers itself is that the electric field is greater at the smaller radius by enough to initiate the avalanche there most of the time; the field variation across the gap is about 10% in the inner chamber where the effect is generally seen. Pairing of sparks opposite one another in succeeding gaps was seen with extreme clearing fields, but the inner-plate mode was the normal condition at the clearing field used, which was selected empirically for maximum gap efficiency.

At track-to-plate-normal angles greater than $\approx 60°$, the resolution is decreased by multiple sparks which occur spread out along the track.

C. Selection of Events

1. Resolution

Event separation was difficult because of the high background. Furthermore the momentum and charge sign of every outgoing particle was unknown, and none of the vertices (production vertex and decay vertices of the Λ^0 and K^0) was seen, except those for occasional decays of neutrals in the active region of the chambers; thus the production angles of all three neutrals were unknown. [The conversion electrons scattered so much in the lead ($\approx 12°$ per electron) that their directions were not useful for providing a measurement of the production vertex.]

Attempts to select events by means of a kinematical calculation plus some simple geometrical checks showed a severe mixing of background (of order 25%); moreover additional ambiguity ($\approx$ 20%) occurred between K^0 and Λ^0 or between p and π^- from Λ^0 decay. The kinematical variable used as the fitting criterion was the angle between the track of the measured proton and the calculated proton, the latter determined kinematically from the angles of the other particles and the beam-track momentum. Hereafter this variable is referred to as the error angle.

Figure 15 shows a distribution of events in the error angle of the best solution with rough checks on the topology and vertex location. The background was intolerable and a simple fitting program was written.

2. Fitting Program

The purpose of the program was reduction of the background to an acceptable level and recovery of events with specific tracks known to be poorly determined.

Errors were assigned to the end points of each track as freedom of motion perpendicular to the track. A standard error was assigned by the program; it depended on the track-plate angle and the length of the tracks. The measurer could specify larger limits on the position of an ill-defined track. The gamma-ray conversion point and the beam track were not movable in the fitting procedure because the fits were insensitive to the former, and the latter were very well determined.

Fitting the $\Sigma^0 K^0$ hypothesis was tried for every possible permutation of the four heavy particles [$\pi^- \pi^+ (K^0)$ and $p \pi^- (\Lambda^0)$]. The

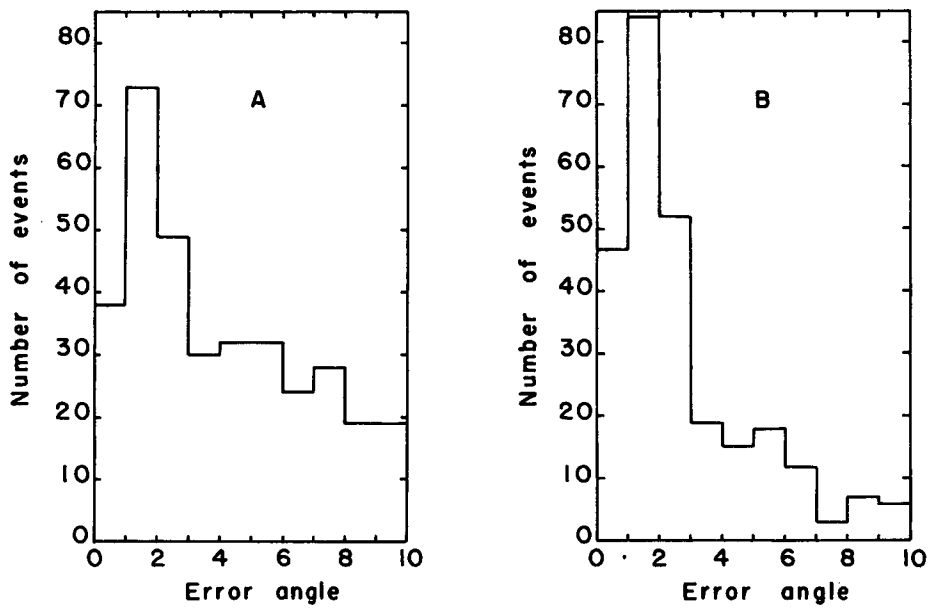

MU-36101

Fig. 15(a). Distribution of events in proton error angle with crude geometrical checks. (b) Distribution of selected events in error angle. (The two distributions do not represent the same size sample.)

events were characterized by two parameters – a chi-squared obtained from kinematical fitting based on adjustment of track-space angles only, and a topological-check parameter based on the translational adjustment of the tracks into the correct topology, but an overall fit to each event was not attempted. The angles of the tracks were believed to be known better than the translational positions.

Computer time was minimized by ending the calculation for a given permutation whenever any of several parameters exceeded a cutoff, for example if the chi-squared just to adjust the tracks into vees was too large; also, quantities calculated for one permutation were saved whenever possible for use with another permutation at the expense of program simplicity. Running time on the UCLRL IBM 7094A was about 4 sec per event.

3. Selection of Events

At first the chi-squared distribution was unexpectedly wide. This effect was found to be caused by small-angle multiple scatters at the lead that were not noticed by the measurers. The multiple Coulomb scattering at the lead was calculated from the computed track momenta. Most events had one or more tracks where the measurer did not detect scattering at the lead but the calculated Coulomb scattering angle was one to ten times the angular error allowed to the track. Let M be the measurement error expected from the rms projected multiple Coulomb scattering angle calculated for a track of given momentum traversing the lead plate. Let E be the angular error allowed to the track measurement by the fitting program. The ratio (R) of M/E (largest value for each event) was strongly correlated with the poorness of fit; it was inferred that measurers were missing small scatters. These events were remeasured under the assumption that such tracks did scatter. Reasonable chi-squared distributions resulted. If the sacttering ratio, R, was greater than 20, that combination of tracks was rejected as impossible, so that the lead provided a crude momentum analysis.

A solution was rejected if the path length of any particle in the hydrogen exceeded its calculated range. This and the scattering ratio limit of the last paragraph proved to be powerful in resolving ambiguous solutions.

Star-like events were rejected if both neutral tracks were calculated to be shorter than 0.2 in.

Finally, any events with ambiguous solutions were rejected.

4. Checking Event Selection with Program FAKE

To check the programs and statistically check the selected events for bias, program FAKE,[9] a Monte Carlo program written to simulate events in the LRL 72-inch bubble chamber, simulated $\Sigma^0 K^0$ events. The multiple-scattering and chamber geometry features of the program were dropped by changing an input code. The experimental geometry was imposed on the Monte Carlo events and they were analyzed by the fitting program. Various problems such as ambiguous solutions were investigated. Various distributions were plotted for the simulated events and compared with the same distributions for the genuine events. The only statistically significant difference between the two sets was an experimental selection bias against long-path-length neutrals – essentially against those decaying in the chambers. Tracks which appear in only two or three gaps before scattering at the lead give poor resolution. The difference disappeared when decays in the chambers were omitted from both sets. Polarization bias cannot be caused by this type of effect, so these events were not omitted from the polarization sample.

The differential cross-section of $\Sigma^0 K^0$ production was estimated by correcting the actual angular distributions with geometrical efficiencies (obtained from the Monte Carlo events) for various production angles; a severe geometrical cutoff was instituted for the purpose of eliminating scanning and triggering biases.

5. Background

The worst type of background event is $\pi^- + p \rightarrow \Lambda^0 + K^0 +$ accidental γ simulated by interaction of the lead with a stray gamma ray or neutron. When this type of interaction passes as $\pi^- + p \rightarrow \Sigma^0 + K^0$, any Λ polarization will cause apparent polarization in the simulated Σ^0's. A search was made for accidental outer-chamber tracks on film of straight-through events at high beam rate. No significant production of this type of track was seen, possibly 1%; a Monte Carlo calculation established the probability of a $\Lambda^0 + K^0 +$ accidental γ faking a $\Sigma^0 K^0$

at 15%, so that the contamination of Λ's should be less than 1%. A $\Lambda^0 K^0 \pi^0$ background is not as troublesome because the Λ's are not likely to be polarized; the probability of faking $\Sigma^0 K^0$ was 20%. With a cross section of only $\approx .01$ mb, contamination from these events should be less than 1%. Most of the background was from stars and quasi-stars (star with one or more secondary scatters) originating mainly in the target walls and chamber plates.

D. Analysis of Selected Events

1. Polarization Analysis by Maximum-Likelihood Method

The Σ^0 polarization (see Sec. II.A.) was analyzed by a maximum-likelihood program for the IBM 7094.

The decay angular distribution of a polarized Λ^0 is

$$I(\cos\theta) = \frac{1}{2}\left[1 + \alpha_\Lambda (\vec{P}_\Lambda \cdot \hat{k}_\pi)\right] , \tag{12}$$

where $\hat{k}_\pi$ is the direction of the decay pion in the Λ center of mass. With this expression, α_Λ is known experimentally to be negative. The Λ polarization is

$$\overline{\langle \vec{P}_\Lambda \rangle} \equiv \vec{P}_\Lambda = -(\vec{P}_\Sigma \cdot \hat{k})\hat{k} , \tag{11}$$

where $\hat{k}$ can refer either to $\hat{k}_\gamma$ or $\hat{k}_\Lambda$ because (11) is bilinear in $\hat{k}$. Combining (12) and (11) gives

$$I = \frac{1}{2}\left[1 - \alpha_\Lambda (\vec{P}_\Sigma \cdot \hat{k})(\hat{k} \cdot \hat{k}_\pi)\right] . \tag{17}$$

Equation (11) is in the center of mass of the sigma and (12) is in the center of mass of the lambda. Equation (17) is permissible providing we measure $\vec{P}_\Sigma \cdot \hat{k}$ in the Σ^0 center of mass. Problems of the relativistic rotation of the Λ^0 polarization vector can be avoided by transforming the Λ^0 and π first into the Σ^0 center of mass and then into the Λ^0 center of mass to evaluate $(\hat{k} \cdot \hat{k}_\pi)$.

We thus write a likelihood function

$$\mathcal{L}(\alpha_\Lambda P_\Sigma) = \prod_i \left[1 - (\alpha_\Lambda P_\Sigma)(\hat{N}_i \cdot \hat{k}_i)(\hat{k}_i \cdot \hat{k}_\pi)\right] , \tag{18}$$

where i denotes the value for the ith event.

2. Differential Cross Sections

Differential cross sections were obtained by correcting the angular distribution with the geometrical efficiencies obtained from the Monte Carlo events. Cosine power-series fits to the production angular distributions were obtained.

IV. RESULTS

A. Cross Sections; Adder Efficiency

This experiment was not designed to provide total or differential cross sections. Total cross sections are difficult to measure because of uncertainty in the triggering efficiency of the adder for the various-sized counters, secondary interactions of particles with the apparatus, and uncertainty in the conversion efficiency of the lead. The total $\Sigma^0 K^0$ cross section, was calculated, however, as a check on the efficiency of the adder; from a lead-conversion efficiency of 22%, appropriate branching ratios, and geometrical efficiencies from the Monte Carlo events, a total cross-section of 0.22 mb averaged over all momenta is obtained. This is in agreement with recent results which indicate a value around 0.24 ± 0.02 (Ref. 10).

Differential cross sections were obtained by selection of events with: (a) no decays in the chambers, to eliminate scanning biases against these; (b) no particles hitting the Lucite side and end pieces of the spark chambers, to eliminate triggering biases caused by particles missing counters and by interactions in these plates and to eliminate scanning biases against particles with oblique track-to-plate angles; and (c) no particles with laboratory angle greater than 90°, to eliminate triggering biases caused by particles missing the counter array. The statistics were especially poor in the forward direction, because forward sigmas produce fast lambdas, which are likely to decay in the chambers, and because backward K^0's tend to have short paths and wide-angle decays. These differential cross sections are presented in Fig. 16 along with those of Anderson[11] and Binford et.al.[10] The data of this experiment at 1275 MeV/c are normalized to 228 μb for comparison with Ref. 10. The data at 1325 and 1365 are normalized to 225 μb for convenience. Cosine power-series coefficients of the curves of Fig. 16 are presented in Table I and plotted against beam momentum in Fig. 17.

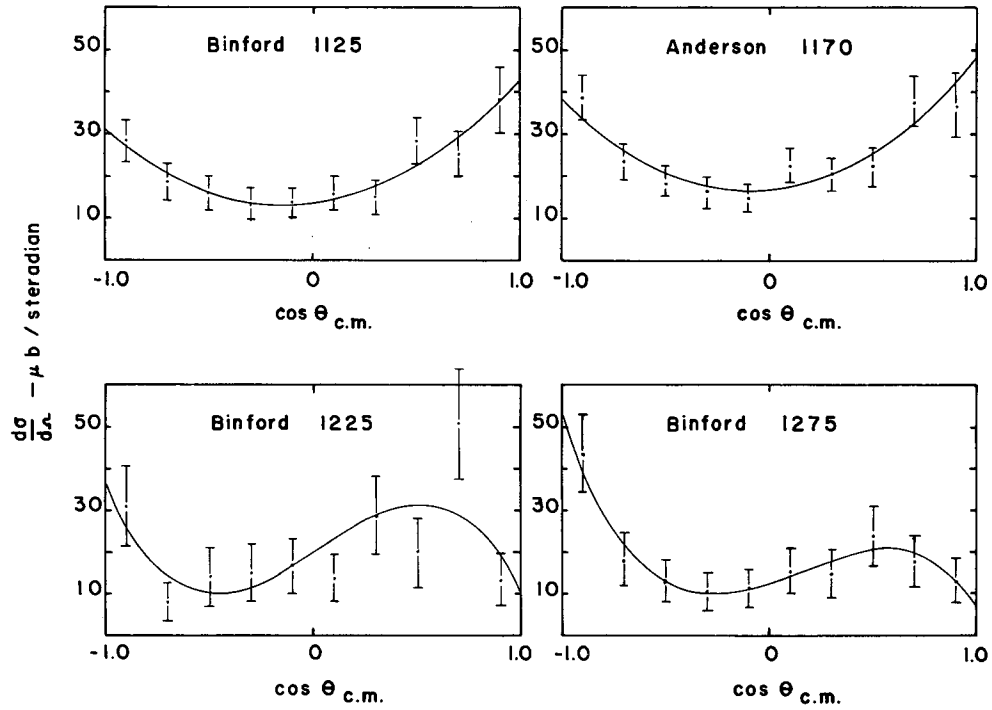
Binford 1125
Anderson 1170
Binford 1225
Binford 1275
50
30
10
-1.0
0
1.0
cos θ c.m.
dσ/dΩ — μb / steradian

MU-36102

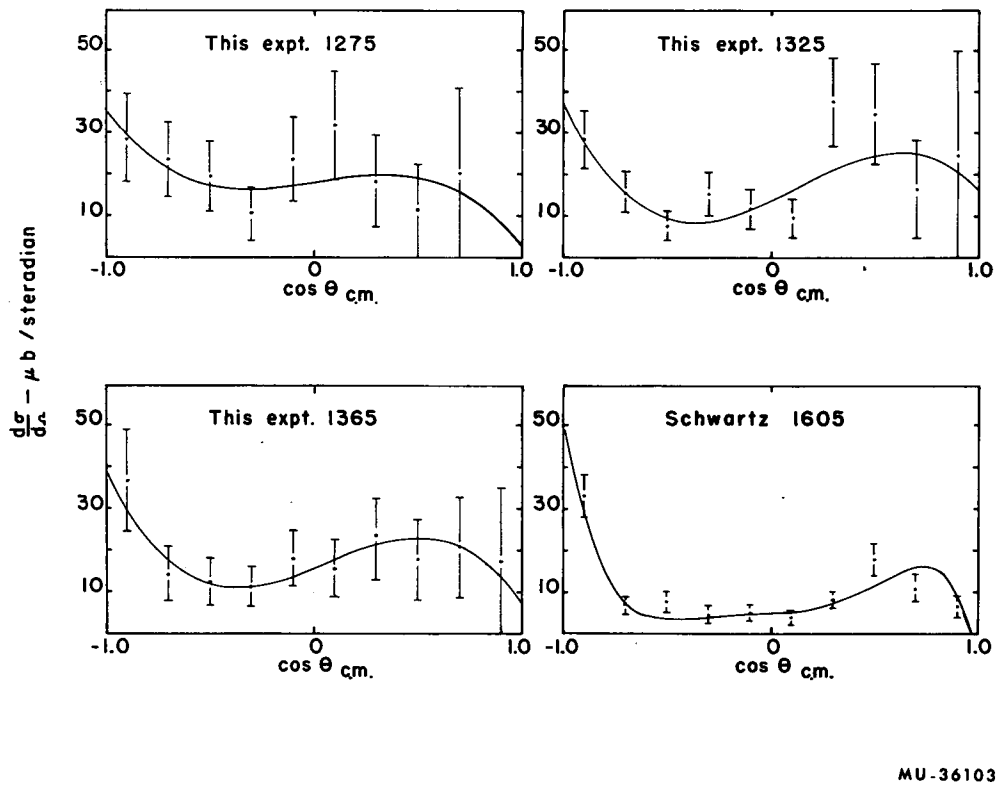

Fig. 16. Differential cross-sections with statistical errors. The curves represent cosine power-series fits from Table I.

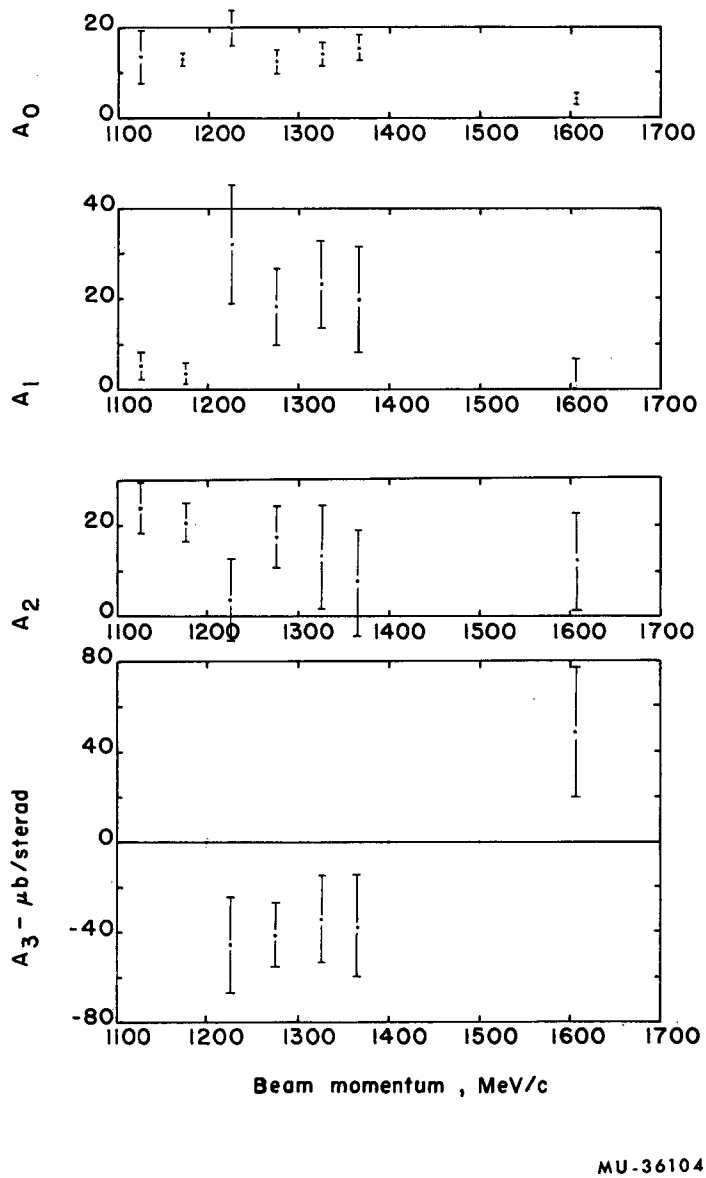

Fig. 17. Coefficients of cosine power-series fit $d\sigma/d\Omega = \sum_L A_L \cos^L \theta$ plotted against beam momentum. The data from which these points were plotted are given in Table I. The points at 1275 MeV/c are from Ref. 10.

Table I. Coefficients of cosine power-series fits.

$\pi^- + p \rightarrow \Sigma^0 + K^0$

p_{π^-}	1125	1170	1225	1275	1275	1325	1365	1605
Coefficient	Binford[a]	Anderson[b]	Binford[a]	Binford[a]	This exp't	This exp't	This exp't	Schwartz[c]
A_0	13.4 ± 5.8	12.8 ± 1.5	19.9 ± 3.9	12.4 ± 2.6	17.7 ± 5.7	13.4 ± 3.0	15.5 ± 3.6	4.4 ± 1.2
A_1	5.7 ± 3.0	3.8 ± 2.2	32.0 ± 13.1	18.3 ± 8.5	8.1 ± 15.9	23.3 ± 9.7	19.9 ± 11.8	0.7 ± 6.3
A_2	23.8 ± 5.7	20.8 ± 4.3	3.6 ± 9.1	17.4 ± 6.9	1.4 ± 23.9	13.4 ± 11.6	7.0 ± 11.8	12 ± 11
A_3			-45.0 ± 20.7	-40.7 ± 14.1	-24.2 ± 37.1	-33.5 ± 19.2	-36.8 ± 22.8	49 ± 29
A_4								6 ± 15
A_5								-77 ± 29
No. of events	d	322	d	d	44	78	50	117
Normalization μb	265 ± 12	248	265 ± 20	228 ± 16	228[e]	225[e]	225[e]	≈ 121

a. Reference 10.

b. Reference 11.

c. Joseph Adam Schwartz, Associated Production from 1.5 to 2.4 BeV/c (Ph. D. thesis), UCRL-11360, June 1964.

d. Blank spaces indicate data not available.

e. Not a measured cross section (see text).

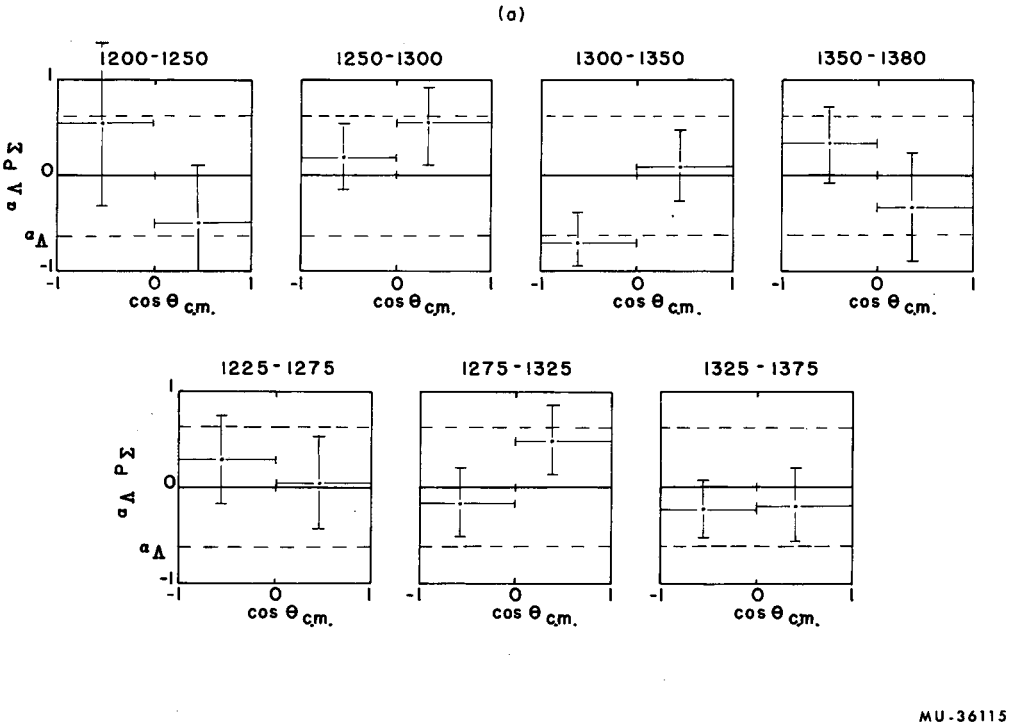
(a)
1200-1250
1250-1300
1300-1350
1350-1380
1225-1275
1275-1325
1325-1375
$\alpha_\Lambda P_\Sigma$
cos θ c.m.
MU-36115

Fig. 18a

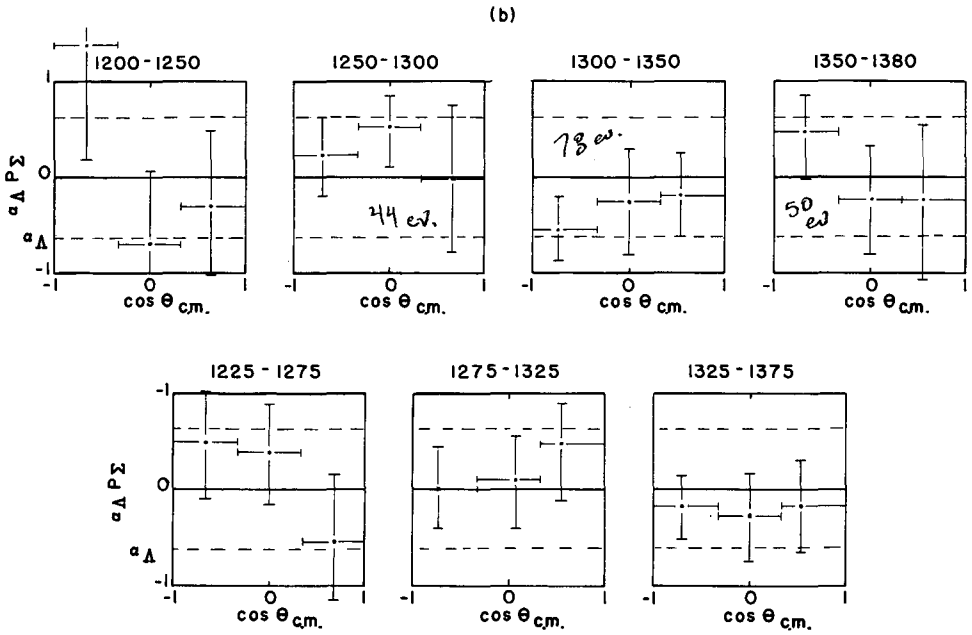

Fig. 18. Polarization results. The values of $\alpha_\Lambda P_\Sigma$ are plotted vs cosine of Σ^0 center-of-mass production angle. The momentum interval is printed above each graph. Errors are the half-widths of the likelihood curves at $1/\sqrt{e}$ of the maximum heights of the curves.

B. Polarization

The Σ^0 polarization results are presented as $\alpha_\Lambda P_\Sigma$ in Fig. 18(a) with the data divided into two production-angle bins and four momentum bins; Figure 18(b) shows the same data for three production-angle bins. The lower row of graphs in each figure (Section a and b) shows the same data with regrouping of momentum bins.

Although the errors are large, there is more structure than would be expected from statistical fluctuations alone if the polarization were small. In particular, asymmetry is noticeable, the polarization displaying sign changes between forward and backward hemispheres of Σ^0 production angle. This effect can be seen in Fig. 19, in which the difference, $\Delta(\alpha_\Lambda P_\Sigma)$, between $\alpha_\Lambda P_\Sigma$ averaged over the forward production hemisphere and $\alpha_\Lambda P_\Sigma$ averaged over the backward production hemisphere is plotted as a function of beam momentum. Between 1200 and 1400 MeV/c, the function appears to go from a large negative value to a large positive value and back to a large negative value, reaching a maximum at about 1300 MeV/c.

C. Discussion of Results

The plots of cosine-series coefficients A_L in the expansion $d\sigma/d\Omega = \sum_L A_L \cos^L \theta$ in Fig. 17 show that A_0 and A_2 are essentially constant, whereas a large A_3 appears suddenly at 1225 MeV/c and A_1 increases simultaneously. The coefficients remain approximately constant to 1400 MeV/c; at 1605 MeV/c a large A_5 term has appeared and A_3 has changed sign.

The differential cross sections at 1125 and 1170 MeV/c are well fit by cosine-series terms to order 2, so they are explainable by s and p waves alone. The sudden appearance at 1225 MeV/c of large A_3 and A_1 coefficients could be caused by interference of s-wave background with the $f_{7/2}$ N^* (1920 MeV). This resonance is centered at 1480 MeV/c in beam momentum and has a half-width of 200 MeV/c. The contribution of an $s^*_{1/2} f_{7/2}$ term to the differential cross section is proportional to $3 \cos\theta - 5 \cos^3\theta$, which is just about the proportion of these terms added to the differential cross section between 1170 and 1225 MeV/c. Although it could be merely a statistical fluctuation, the rapid change

in polarization with beam momentum between 1200 and 1400 MeV/c suggested by the data of Fig. 19 is at variance with this picture because the polarization should not change rapidly if the dominant interaction term consists of a slowly rising resonant amplitude interfering with a slowly varying background term.

The momentum dependence of $\Delta(\alpha_\Lambda P_\Sigma)$ in Fig. 19 suggests that at least one other strong amplitude is active near 1300 MeV/c. The existence of a large $d_{5/2}$ amplitude would fit the $\Sigma^0 K^0$ production data in several ways. The angular distribution at 1225 MeV/c would be explainable in terms of $p_{1/2} d_{5/2}$ interference, which gives the same angular distribution as $s_{1/2} f_{7/2}$ interference. Rapidly varying polarization could be more readily explained. The large $\cos^5$ angular-distribution coefficient at 1605 MeV/c could be explainable as interference of $d_{5/2}$ with the 1920 MeV $f_{7/2} N^*$ amplitude. The angular distributions obtained at 1325 and 1365 MeV/c are not precise enough to exclude a substantial A_5 coefficient of the sign found at 1605 MeV/c because there is a strong negative correlation between A_3 and A_5 in the coefficient error matrix. Interference of $d_{5/2}$ and $f_{7/2}$ could thus already be present at 1325 and 1365 MeV/c. In any event at least four partial waves are evidently required to fit the available data; a conclusive phase-shift analysis in this momentum region will require more precise angular distributions and polarization measurements and should, of course, include information from elastic scattering and other inelastic channels.

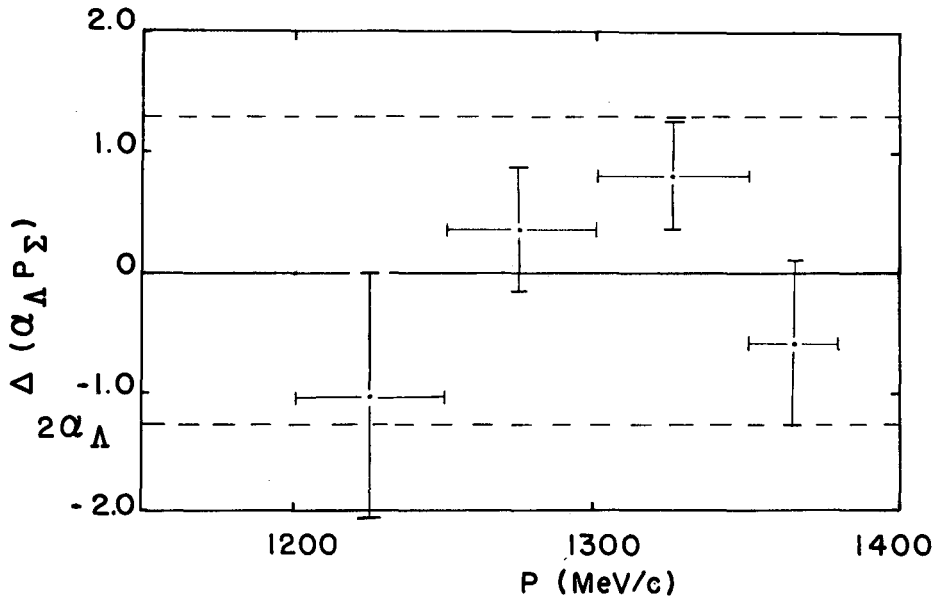

MU-36117

Fig. 19. Difference between $\alpha_\Lambda P_\Sigma$ for forward Σ^0 production hemisphere and $\alpha_\Lambda P_\Sigma$ for backward hemisphere plotted vs pion-beam momentum.

V. CONCLUSIONS

World statistics on Σ^0 K^0 production in the region 1200 to 1500 MeV/c are weak, partly because the cross section is low and partly because gamma rays are not detected in most hydrogen bubble chamber Σ^0 K^0 events. The $\Sigma\Lambda$ parity determinations to date agree but are not unchallengeable;[7,8] there is little interest in this problem now, however, because of the measurements to date plus the successes of the group-symmetry theories that put Σ^0 and Λ^0 in the same supermultiplets with common parity.

The general problem of poor Σ^0 K^0 statistics is probably soluble by a spark-chamber experiment in which the adder technique of this experiment is used despite the intense background encountered. Increasing the number of events by a factor of ten would justify such an experiment. The geometrical efficiency of this experiment was only $\approx$ 25% for complete events on the loose triggering mode (no UD counters), and gamma-conversion efficiency was only $\approx$ 20%. The target depth could probably be doubled. The number of events could thus in principle be increased by a factor of 40 with a disproportionately small increase in background. Better resolution and larger chambers might also save events with K_2^0 decays.

This experiment would have yielded twice the number of Σ^0's had loose triggering been used throughout, and could have yielded another factor of 1.5 by the use of a larger inner chamber to improve resolution and scanning efficiency for neutral decays downstream of the target. Background triggers could have been reduced by $\approx$ 30% by extensive anticoincidence counters around the insensitive solid angle, a measure that was not taken in the hope of resolving events with a lost K^0 decay pion.

A further significant improvement could have been obtained with a 270° (or 3/4) cylindrical spark chamber. Such a chamber was constructed and tested but was rejected because light-reflection attenuation was too high. Achieving better polish, e. g., by chrome plating, would make such a chamber feasible; track images would still be no worse then hyperbolic.

One could, however, do still better with a radically redesigned experiment. The use of streamer chambers would provide several advantages. Their isotropic nature would avoid loss of resolution from tracks making oblique angles with the plates of ordinary spark chambers; this problem, important for large solid-angle detection, was noticed even with the cylindrical geometry of this experiment. Streamer chambers show no loss of efficiency for high-multiplicity tracks. When fine wire-grid electrodes are used, streamer-chamber tracks can be photographed from any direction and even through other chambers.

Low light output is a disadvantage of streamer chambers that may yield to study. Photographs are currently being taken at f/2.5 with ± 0.2-mm track resolution in both directions.[12]

Bubble-chamber measuring devices and event-processing codes are readily adaptable to streamer chambers with or without magnetic field.

ACKNOWLEDGMENTS

It has been a pleasure to work in the atmosphere of cooperation which characterizes this Laboratory. I would like to thank Dr. E. J. Lofgren for the hospitality of his group. The guidance and example of Dr. Bruce Cork, Professor Leroy Kerth, and Dr. William Wenzel have been the most necessary ingredients for the successful completion of my graduate work. They and Drs. Victor Cook, William Layson, and Denis Keefe participated in the experiment. I am also indebted to the Bevatron crew and the technicians of the Lofgren Research group. Numerous scanners have put in hard hours on this experiment. Mr. Rolland Johnson has contributed extensively to the data organization and computer analysis.

This work was done under the auspices of the U. S. Atomic Energy Commission.

APPENDIX

Calculation of the Number of Dalitz Decays Required to Measure the $\Sigma\Lambda$ Parity

Dalitz pair decays of the Σ^0 have been simulated according to Eq. (15) by a Monte Carlo program for the IBM 7094. The distribution of likelihood ratios for experiments containing as many as 200 events has been obtained for five values of sigma polarization. No approximations were made beyond the averaging used to obtain Eq. (15); however, it has been assumed that the sigma polarization and all angles are known exactly.

Random-number generation of four angles per event is sufficient to determine the event: the decay cosine of $(\vec{P}_\Sigma, \vec{k}_\Lambda)$ and the orientation angle of the Dalitz plane determine $\vec{P}_\Lambda$ by Eq. (15); the decay cosine [distributed according to Eq. (12)] and the azimuthal orientation of the lambda-decay plane determine $\vec{k}_\pi$. The likelihood function is

$$\mathcal{L} = \prod_i (1 + \alpha_\Lambda \vec{P}_\Lambda \cdot \hat{k}_\pi) ,$$

and the likelihood ratio is

$$R = \frac{\mathcal{L}(-)}{\mathcal{L}(+)} ,$$

where the - and + refer to the even and odd parity choices of Eq. (15). The events were generated according to the even-parity choice.

The median logarithm of the likelihood ratio vs the number of events N in the samples is plotted as the central curve in each section of Fig. 20. (A separate graph is presented for each of five values of P_Σ.) The probability of the result of an experiment falling within the envelope equals the odds against exceeding one standard deviation. The curves are well represented by the formula

$$\text{Log } R = \frac{P_\Sigma}{2} \left(\frac{N}{20} \pm \sqrt{\frac{N}{20}}\right) .$$

Forty-two thousand events were generated and analyzed for each of the five graphs. The computer running time was three minutes per graph.

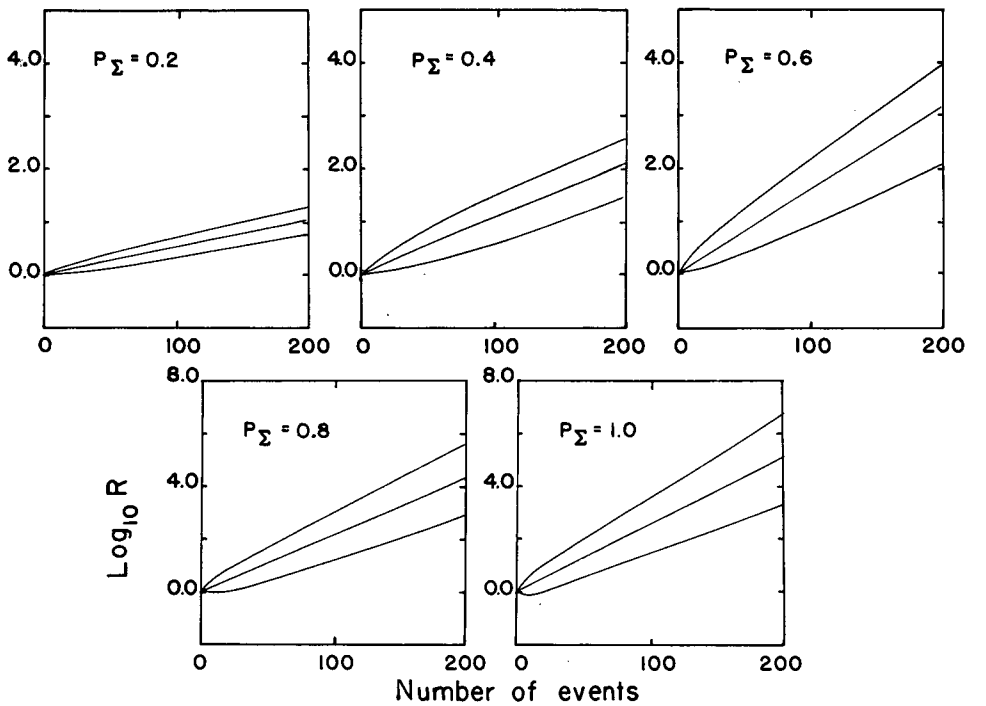

MU-36105

Fig. 20. Distribution of the logarithm of the likelihood ratio, R, expected for a $\Sigma\Lambda$ parity measurement as a function of the number of events in the sample is given by the central curve. The rms spread in $\log_{10}R$ for samples of N events is given by the vertical width of the envelope (distance between top and bottom curves).

REFERENCES

1. R. Gatto, Phys. Rev. 109, 610 (1958).
2. G. Feinberg, Phys. Rev. 109, 1019 (1958).
3. Gordon Feldman and Thomas Fulton, Nucl. Phys. 8, 106 (1958).
4. J. Sucher and G. A. Snow, Nuovo Cimento 18, 195 (1960).
5. Nina Byers and Hugh Burkhardt, Phys. Rev. 121, 281 (1961).
6. B. N. Valuev and B. V. Geshkenbeĭn, Sov. Phys. JETP (English trans). 12, 728 (1961).
7. H. Courant, H. Filthuth, P. Franzini, R. G. Glasser, A. Minguzzi-Ranzi, A. Segar, and W. Willis and R. A. Burnstein, T. B. Day, B. Kehoe, A. J. Herz, M. Sakitt, B. Sechi-Zorn, N. Seeman, and G. A. Snow, Phys. Rev. Letters 10, 409 (1963).
8. Mason B. Watson, Massimilliano Ferro-Luzzi, and Robert D. Tripp, Phys. Rev. 131, 2248 (1963).
9. Gerald R. Lynch, Program FAKE: Monte Carlo Simulation of Bubble Chamber Events, UCRL-10335, July 10, 1962.
10. Thomas O. Binford (Physics Department, Univ. of Wisconsin), private communication, April 1965. Collaborators include Gordon Lind, V. G. Lind, and D. Stern.
11. Jared Arnold Anderson, Strange Particle Production by 1170 MeV/c π^- Mesons (Ph.D. Thesis), UCRL-10838, May 1963.
12. Francisco Villa (Stanford Linear Accelerator Center, Stanford, California), private communication, April 1965.

This report was prepared as an account of Government sponsored work. Neither the United States, nor the Commission, nor any person acting on behalf of the Commission:

A. Makes any warranty or representation, expressed or implied, with respect to the accuracy, completeness, or usefulness of the information contained in this report, or that the use of any information, apparatus, method, or process disclosed in this report may not infringe privately owned rights; or

B. Assumes any liabilities with respect to the use of, or for damages resulting from the use of any information, apparatus, method, or process disclosed in this report.

As used in the above, "person acting on behalf of the Commission" includes any employee or contractor of the Commission, or employee of such contractor, to the extent that such employee or contractor of the Commission, or employee of such contractor prepares, disseminates, or provides access to, any information pursuant to his employment or contract with the Commission, or his employment with such contractor.